MODELING AND EXPERIMENTAL STUDY OF LITHIUM-ION BATTERY THERMAL BEHAVIOR

A Thesis

by

CARLOS FELIPE LOPEZ

Submitted to the Office of Graduate and Professional Studies of
Texas A&M University
in partial fulfillment of the requirements for the degree of

MASTER OF SCIENCE

Chair of Committee,	Partha P. Mukherjee
Committee Members,	Debjyoti Banerjee
	Raktim Bhattacharya
	Judith A. Jeevarajan
Head of Department,	Andreas A. Polycarpou

May 2015

Major Subject: Mechanical Engineering

ABSTRACT

While the popularity of lithium-ion batteries (LIBs) has increased significantly in recent years, safety concerns due to the high thermal instability of LIBs limit their use in applications with zero tolerance for failure. A safety issue of particular interest is a scenario called thermal runaway in which several exothermic side-reactions occur at elevated temperature ranges and release heat, which can then trigger the next reaction. This matter worsens when multiple cells are installed in close proximity to each other as the released heat from an abused cell can activate the chain of reactions in a neighboring cell, causing an entire module to heat rapidly and vent or ignite. This body of work aims to study LIB thermal behavior using both modeling and experiments to determine design practices that improve the safety of LIB modules. Based on the results of single cell abuse testing, a numerical model of the side-reactions that occur during thermal runaway was developed. The results showed that cell form factor and ambient conditions influence abuse behavior significantly. These abuse tests were extended to multi-cell modules to determine the effect of cell spacing, electrical configuration, and protection materials on the propagation of thermal runaway from an abused cell to a surrounding one. Lastly, an electrochemically coupled thermal model of battery thermal management systems of various configurations was created. An optimum thermal management design was found that utilized both active and passive methods of cooling to keep cell temperatures and thermal gradients within safe limits. The work described herein is expected to provide insight into safe battery design practices.

ACKNOWLEDGEMENTS

I would like to thank my committee chair, Dr. Mukherjee, and my committee members, Dr. Banerjee, Dr. Bhattacharya, and Dr. Jeevarajan, for their guidance and support throughout the course of this research.

I also want to extend my gratitude to the NASA Propulsion and Power Division at Johnson Space Center and the NASA Office of Education for the opportunity and funding for this work. The assistance of the Energy Systems Test Area personnel at NASA-JSC was invaluable and greatly appreciated. Thanks also go to my friends and colleagues at the Energy and Transport Sciences Lab for their assistance and company.

TABLE OF CONTENTS

Page

LIST OF FIGURES

Page

LIST OF TABLES

Page

1. INTRODUCTION

As the energy and power densities of lithium-ion batteries (LIBs) continue to increase, the risk associated with thermal safety of LIBs increases as well. Off-nominal operating conditions such as mechanical abuse, short circuit, over-charge, and high temperatures can lead to critical failure of lithium-ion cells [1-4]. These abuse conditions can initiate thermal runaway within a cell wherein a chain reaction of exothermic side-reactions can cause a cell to reach temperatures of over 600 °C. This reaction sequence typically involves solid-electrolyte interphase decomposition, anode/cathode reactions with the solvent, and the vaporization or the potential combustion of the electrolyte [5-7]. Various safety features including vents, flame retardant additives, current interrupt (CID) and positive thermal coefficient (PTC) devices can minimize the probability and severity of a thermal event on a cell level [8-10]. The relative thermal stability of lithium-ion batteries also varies with electrode material composition [11, 12], manufacturing method [13], and separator materials [14, 15]. An in depth understanding of the thermal behavior during abuse conditions is required to improve the safety of lithium-ion batteries [16, 17].

Lithium-ion batteries are constructed with an anode, cathode, separator, current collectors, and electrolyte, shown in Figure 1. During normal operation, lithium ions move via diffusion and migration from one electrode to the other through the electrolyte and separator [4]. The electrons associated with each lithium-ion move through the current collector of one electrode, travel through the external load, and terminate at the

opposite electrode, performing electrical work in the process. The cells considered in this work are spiral wound cells which are manufactured by winding a long sheet of the component layers into a spiral and inserting said sheet into a cylindrical or prismatic can.

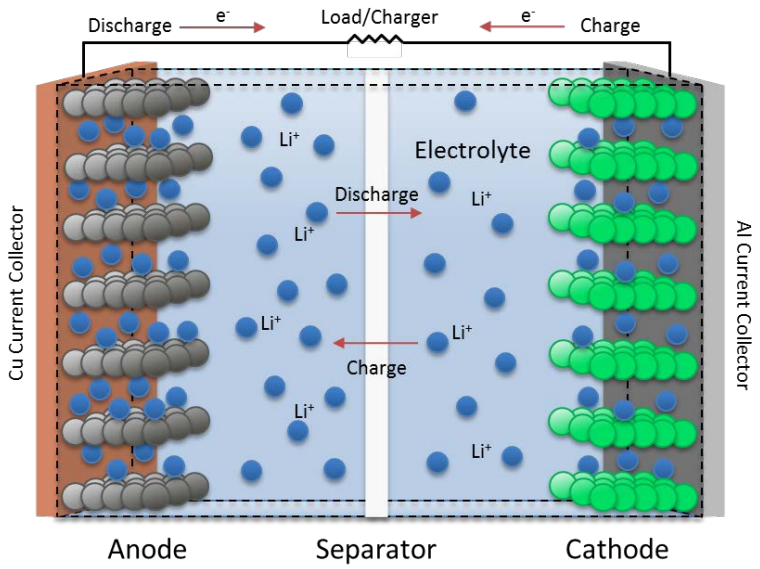

Figure 1. Components of a typical lithium-ion battery with current collectors, electrodes, separator and electrolyte.

1.1 Mechanisms of Thermal Runaway

The thermal behavior of lithium-ion batteries under normal operation has been studied extensively and can be modeled using a coupled thermal-electrochemical model [18, 19]. A different formulation that captures the side-reactions that occur at elevated temperatures is required to capture abuse behavior and determine safe practices. Many researchers have studied the mechanisms of thermal runaway in an attempt to determine

methods of improving LIB safety. Spotnitz and Franklin [20] summarized a general progression of the exothermic reactions that contribute to thermal runaway. First, the solid-electrolyte interphase (SEI) layer, which protects the anode active material from direct reaction with the electrolyte solvent, will begin to decompose at 90 to 120 °C. Using accelerated rate calorimetry (ARC) and differential scanning calorimetry (DSC), it has been shown that the SEI reaction peaks at a temperature of 100 °C [21, 22]. The generated heat is caused by the decomposition of the meta-stable component of the SEI layer and decreases as this species is consumed. It was shown that the heat release was independent of the amount of intercalated lithium but was very sensitive to the surface area of the anode, as this increased the amount of meta-stable SEI [23]. This reaction is expected to be of the form

$$\left(CH_2OCO_2Li\right)_2 \rightarrow Li_2CO_3 + C_2H_4 + CO_2 + \frac{1}{2}O_2 \qquad (1)$$

where $\left(CH_2OCO_2Li\right)_2$ is the meta-stable component and Li_2CO_3 is the stable component of the SEI layer.

Once the SEI layer decomposes, it no longer protects the graphite the intercalated lithium in the anode will begin to react with the electrolyte solvents at temperatures greater than 120 °C. Richard and Dahn [21] and Biensan et al [24] analyzed the thermal stability of intercalated graphite and found a heat release peak at 120 °C, although the exact peaks vary with the solvents used in the electrolyte. Some possible reactions of intercalated lithium with electrolyte solvent include

$$2Li + C_3H_4O_3\left(EC\right) \rightarrow Li_2CO_3 + C_2H_4 \qquad (2)$$

$$2Li + C_3H_6O_3(DMC) \rightarrow Li_2CO_3 + C_2H_6 \quad (3)$$

$$2Li + C_4H_8O_3(EMC) \rightarrow Li_2CO_3 + C_3H_8 \quad (4)$$

where the contribution from each reaction will vary with the content of each solvent in the electrolyte.

The first two reactions in the anode can heat the cell to temperatures where the positive active material can decompose and release oxygen and/or react with the electrolyte solvent, beginning at approximately 170 °C. The activation energy, reaction enthalpy, and frequency factor for the LCO positive-solvent reaction have been measured using ARC and x-ray diffraction by MacNeil and Dahn [25]. These researchers also compare the thermal stability of numerous other charged cathode materials, though they only report onset/peak temperature and heat release [26]. Kong et al. [27] showed that the gases released from the cathode during normal operation was independent of the cathode material, but did vary among LCO, LMO, and LFP when cells were overcharged. The cathode reaction is characterized by decomposition and release of oxygen followed by possible combustion with the electrolyte solvents shown as

$$Mn_2O_4 \rightarrow Mn_2O_3 + \frac{1}{2}O_2 \quad (5)$$

$$3O_2 + C_3H_6O_3(DMC) \rightarrow 3CO_3 + 3H_2O \quad (6)$$

for LMO spinel cathode and dimethyl carbonate electrolyte solvent.

Lastly, any electrolyte that remains after the reactions with the negative and positive electrodes can decompose at temperatures greater than 200 °C. The heat

generated from electrolyte decomposition combined with heat released during combustion with released oxygen can elevate cell temperatures to over 600 °C. Previous work has shown that the thermal stability of $LiPF_6$-EC:EMC electrolyte is dependent on component concentrations and heating rate using DSC [24, 28]. The exact decomposition reaction, trigger temperature, and released heat are dependent on the solvent in question [29].

Abuse testing cells by subjecting them to off-nominal conditions can provide valuable insight into the probability and severity of a thermal runaway scenario. Various abuse conditions including overcharge, short-circuit, nail penetration, and oven tests each provide a different avenue to a runaway reaction [3]. As a standard test for cell safety, oven tests in particular are able to characterize the trigger temperature and heat released during a thermal event for a single cell. Since experimental testing is costly, researchers often look to numerical modeling to study thermal abuse behavior of lithium-ion cells. Using experimental oven test data and reaction parameters acquired via calorimetry, Hatchard et al. [30] created a one-dimensional oven test model for both 18650 cylindrical and prismatic cells. The model accurately captured the effect of cell size, electrode material, surface area of the anode, and cell surface emissivity on cell temperature and was verified with experimental data [31]. Spotnitz et al. [20] developed a model that simulated more abuse scenarios including oven test, short-circuit, overcharge, nail penetration, and crush test for multiple cathode materials. This work reports that reactions of the binder are insignificant when compared to the other reactions. Kim et al. [32] then expanded the one-dimensional thermal abuse model to

three dimensions to capture the effect of large-cell geometry and spatial variance in temperature. They found that for large cells local hot spots can form that trigger thermal runaway sooner than predicted with 1-D or lumped models. Since small cells are able to reject heat faster than large format cells, the internal temperature gradients of large prismatic cells are critical to the modeling of thermal runaway. Guo et al. [33] also developed a three-dimensional thermal abuse model that included both LCO and LFP cells ranging from 18650 cylindrical cell to large format (55 Ah) cells for electric vehicles. Spotnitz [34] expanded the abuse model to three dimensions as well, and showed that cells in contact with each other were more likely to go into thermal runaway. Additionally, Peng et al. [35] outlined the significance of the surface heat transfer condition on thermal runaway onset and severity.

Performing an oven test does not provide much insight into the safety of a multi-cell module as the heat transfer from a triggered cell to adjacent cells is of particular interest. To determine the probability of thermal runaway propagation, a constant-power single-cell heating test, or modified oven test, is often performed. This test generally consists of heating a “trigger” cell within a multi-cell module until thermal runaway is achieved. The propagation of this condition can then be studied using module of various configurations to determine safe module designs.

1.2 Propagation of Thermal Runaway

In many cases, battery designers are concerned with not only the onset of thermal runaway in one cell, but the propagation of thermal runaway to cells in close proximity to the cell experiencing abuse [13]. The heat released from the exothermic reactions

occurring in one cell can subsequently heat the adjacent cells, causing them to heat rapidly, causing a cell-to-cell chain reaction. The potential for this module-level thermal runaway scenario must be avoided, especially in applications where safety is paramount such as in the aerospace and automotive industries. The aforementioned CID and PTC safety devices along with flame retardants can help reduce the chance of thermal runaway propagation [8, 9, 36, 37]. Many researchers have studied the parameters that influence the onset of thermal runaway in order to improve LIB safety [20, 38, 39]. The effect of battery materials and manufacturing techniques on thermal behavior has been analyzed in several studies [12, 15-17, 22, 40]. However, experimental abuse testing of LIB modules is often used to determine thermal behavior in-situ [30].

As many modules are assembled from with smaller cells, this propagation scenario can be disastrous in many applications. Each cell that is added to a thermal runaway reaction contains additional energy to fuel the fire [41]. Typically, designers are under pressure from the customers to design modules that are as small and lightweight as possible, increasing energy and power density. Sometimes cells are installed with less than 1 mm of spacing between them, or even installed in contact with adjacent cells. Such modules experience particularly severe runaway reactions, so it would be desirable to increase the cell separation from a safety standpoint. In addition, modules with banks of cells in parallel present another safety concern. Should one cell experience an internal short due to physical damage or melting of the separator, it can act as a short for the entire bank, leading to an external short condition for the remaining cells. This can rapidly heat the adjacent cells because of the rapid rate of discharge, leading to parallel

configurations being inherently less safe than series strings. The configuration of the bank tabs could be selected such that a short caused by an abuse condition would not affect the entire bank. The electrolyte vapor and fire released from cell vents could also contribute to heating of adjacent cells, indicating that the direction of expelled vapor and fire needs to be controlled by the module design.

Various thermal insulation materials such as radiant barriers or intumescents could provide protection from vented electrolyte. A radiant barrier provides protection from direct flame and reduces the rate of radiative heat transfer, as shown in the subsequent analysis. This is particularly useful in protecting cells as an abused cell can reach over 600 °C, where radiation heat transfer becomes quite important. Intumescent materials have been used extensively to add fire protection to structural members in building construction [42-44]. These materials chemically react at elevated temperatures to transform from a thermoplastic to a dense insulating ash or char [45-47]. The exact mechanism of this reaction varies with the chemical composition of the intumescent and the plastic carrier it is suspended in [48, 49]. Once this chemical reaction occurs, the dense ash could protect the cells from direct flame released from an abused cell. Some researchers have even proposed that flame retardants be added to cell internal components, increasing safety at the cost of decreased capacity [50].

1.3 Thermal Management

While understanding the mechanism of thermal runaway and propagation is important for designing abuse tolerant batteries, another approach is to preemptively manage battery temperatures before thermal runaway can even occur. Battery thermal

management systems (BTMS) can often dissipate heat before the cell temperatures can reach thermal runaway range. However, these systems come at the cost of increased volume and weight which need to be minimized in the aerospace and automotive industries [51, 52]. Thermal runaway protection aside, proper battery thermal management is still critical to the performance and life of LIB modules. For example, prolonged exposure to elevated temperatures can lead to capacity and power loss due to the electrochemical dependence on temperature [1]. Capacity fade occurs when the active materials in a cell react with other components, consuming available lithium and blocking intercalation sites. These reactions also decrease the available power due to the increase in internal impedance which reduces cell voltage. The rates at which these reactions occur are exponential functions of temperature, and thus, increase greatly at temperatures higher than approximately 50 °C. It is for this reason that battery manufacturers specify a maximum operating (charge/discharge) temperature ranging from 40 to 50 °C. Additionally, internal and cell-to-cell thermal gradients can cause an imbalance in cell performance and capacity, leading to module-level performance issues such as premature capacity fade in areas of high gradient [53]. Local current density and state-of-charge are functions of temperature and therefore become more polarized as temperature gradients increase, leading to local preferential cycling and decreased capacity [54]. To make matters worse, off-nominal abuse conditions such as overcharge, short circuit, and mechanical abuse can cause a series of exothermic side reactions to occur, each fueling the next reaction, leading to extremely high temperatures in a condition called thermal runaway [30, 35]. This presents a dangerous scenario where

vaporized electrolyte can ignite and adjacent cells can be affected, leading to an entire battery module reacting. Because safety is paramount in applications using LIBs, researchers are actively engaged in furthering the understanding of LIB thermal behavior [1, 55].

Battery thermal management systems (BTMS) are commonly used to control battery temperatures and prevent accelerated capacity fade and performance degradation [56]. These thermal management systems employ the use of various heat transfer and fluid flow mechanisms to remove heat from the cells [57]. Conduction and convection dominate these systems as radiation often has an insignificant effect on the operational temperature window, but becomes more important in situations when thermal runaway is triggered. Thermal management techniques are often grouped into active and passive systems [58]. Active systems involve the use of forced convection to dissipate the heat generated during cell operation. The heat transfer fluid can be air, water, ethylene glycol, and other coolants. Passive devices either use natural convection or latent heat storage to reject heat from the cells. Phase change materials (PCMs) that melt in the 40-60 °C range are commonly used for passive thermal management [59]. Active systems require external energy input to drive the fan or pump and are often more expensive than passive systems.

Active systems can be further classified into direct and indirect categories. In direct active systems, the heat transfer fluid is in direct contact with the cells. A typical case would be when air is used as the cooling fluid where the low heat transfer resistance due to direct contact counteracts the relatively low thermal conductivity and heat

capacity of air. Indirect systems use some intermediate material that creates a conduction pathway for the heat to be transferred from the cells to the coolant. The direct method is preferred because it provides the least restrictive avenue for heat dissipation. However, since batteries are electrical systems, the coolants used in a direct method must exhibit sufficiently low conductance and capacitance. This requirement limits the coolant choice to air or mineral oil, both of which have lower thermal conductivity and heat capacity than water or ethylene glycol. Therefore, active cooling methods are generally limited to the inexpensive, lightweight, but poorer performing direct air cooling or the more costly, more massive, and better performing indirect liquid cooling systems. Table 1 compares the relevant properties of various coolants used in active cooling systems.

Table 1. Coolant properties evaluated at standard temperature and pressure [60].

Coolant	Density (kg/m^3)	Specific Heat (kJ/kg-K)	Thermal Cond. (W/m-K)	Viscosity (cP)
Water	1000	4.179	0.58	0.89
Ethylene glycol (60%)	1081	3.147	0.36	4.23
Mineral oil	838	1.67	0.162	15.3
Air	1.127	1.005	0.0271	0.0186

In passive cooling systems, heat dissipation can be provided via natural convection using ambient air, or latent heat using phase change materials [61, 62]. For larger modules that are typically of interest when discussing thermal issues, natural convection does not by itself provide enough dissipation to maintain the required temperatures, even when a finned heat sink is used. Phase change materials, however,

provide an interesting alternative passive method. These materials are selected to undergo a phase transition near the upper limit of recommended operating temperature, typically 40 to 50 °C [63, 64]. Since these materials melt and often increase in volume, they are typically encapsulated in a graphite or polymer matrix to maintain their solid construction after phase change [65, 66]. The thermal conductivity, melting range, heat capacity, and latent heat for selected phase change materials are shown in Table 2 [67]. The melting range and latent heat requirements for a BTMS narrows the suitable PCMs to a select few, most commonly paraffin wax and lauric acid encapsulated in graphite [68]. It is expected that these properties will have a significant effect on the performance of passive BTMS using PCMs.

Table 2. Thermo-physical properties of typical phase change materials [62, 63, 67].

Material	Melting Range (°C)	Latent Heat (kJ/kg)	Thermal Cond. (W/m-K)	Specific Heat (kJ/kg-K)	Density (kg/m^3)
Paraffin wax	42-45	123	16.6	1.98	789
Lauric acid	41-43	211.6	1.6	1.76	1007
None (air)	-	-	0.0271	1.005	1.127

As the size of battery modules increases, an adequately designed BTMS becomes highly critical for the protection of the module because increasing the number of cells increases the heat generated during operation, which must be rejected to the surroundings via a BTMS. Therefore, it can be expected that module configuration has a significant effect on the performance of active and passive thermal management

systems. Factors such as cell form factor, inter-cell spacing, module operation cycle, module electrical configuration [2], coolant/PCM properties, coolant/PCM physical construction, and ambient conditions all affect the performance and safety of a LIB module. Due to the various external conditions that can affect the thermal response of a battery module, it is important to consider both the electrochemical properties of the individual cells and the thermal characteristics of the surrounding thermal management system in three-dimensions [19, 69].

2. ABUSE TESTING AND MODELING

The objective of this section is to model the thermal behavior of cells of cylindrical spiral-wound and prismatic spiral wound cells subjected to elevated temperatures via this modified oven test. This model will eventually allow for the prediction of thermal runaway propagation in multi-cell modules using the studied cells. The cells studied in this section consist of a $LiCoO_2$ cathode, graphite anode, and $LiPF_6$/EC:EMC:DMC electrolyte, shown in Figure 2. The first cell of interest is a cylindrical spiral-wound cell of the 18650 design that has a capacity of 2.8 Ah, charge voltage of 4.3 V, discharge cutoff voltage of 3.0 V, a diameter of 18 mm, and height of 65 mm. The second cell is a prismatic spiral-wound cell that has a capacity of 5.3 Ah, charge voltage of 4.2 V, discharge cutoff voltage of 2.75 V, a length of 37.3 mm, width of 19 mm, and height of 64.8 mm. While both of these cells use the LCO cathode material, differences in the manufacturing process, thermal mass, and vent location cause their abuse behavior to differ.

2.1 Thermal Abuse Model

The thermal energy conservation equation governs the behavior of the cells during the thermal abuse test and is given as

$$\rho c_p \frac{\partial T}{\partial t} = \nabla \cdot k \nabla T + Q_{gen} \tag{7}$$

where ρ (kg m^{-3}) is the cell density, c_p (J kg^{-1} K^{-1}) is the specific heat capacity of the cell, T (K) is the temperature, t (s) is time, k (W m^{-1} K^{-1}) is the cell thermal

(a) Cylindrical (b) Prismatic

Figure 2. (a) Cylindrical spiral-wound test article with flexible heater element installed before and after the modified oven test. (b) Prismatic test article with heater element installed before and after the modified oven test.

conductivity, and Q_{gen} ($\mathrm{W\,m^{-3}}$) is the total heat generation from the various side reactions occurring during the abuse test. The thermo-physical properties of the various cell components are given in Table 3. The complete cell properties are evaluated using weighted averaging and are taken to be isotropic with the exception of thermal conductivity, which is anisotropic in nature due to the layering of the cell components.

Since the energy conservation equation is solved numerically in the radial direction, the thermal conductivity is calculated by the expression

$$k_n = \frac{\sum_i l_i}{\sum_i l_i / k_i} \tag{8}$$

where k_n (W m^{-1} K) is the normal direction thermal conductivity, l_i (m) is a layer's thickness, and k_i (W m^{-1} K) is a layer's thermal conductivity, taken from Table 3.

The boundary conditions of the cell are taken to be the no flux condition along the center axis of the cells and the convection condition plus heat flux from the heater on the external surfaces of the cells, given as

$$q''_{conv} = h\left(T_{can} - T_{amb}\right) - \frac{IV}{A_h} \tag{9}$$

where q''_{conv} (W m^{-2}) is the boundary convective heat flux, h (W m^{-2} K^{-1}) is the convection heat transfer coefficient, T_{can} (K) is the can surface temperature, T_{amb} (K) is the ambient temperature, I (A) is the heater current, V (V) is the heater voltage A_h (m^2) is the heater contact area. During conventional oven testing, the convection coefficient is considered to be approximately a constant value as actively controlled blowers maintain the oven temperature and the heater is not used. In the modified oven test, the resistive heater is the primary source of heat and is considered to be a heat flux into the cell. At elevated temperatures, radiation heat transfer from the cell is also considered as a boundary condition, given as

$$q''_{rad} = \varepsilon\sigma\left(T_{can}^4 - T_{amb}^4\right) \tag{10}$$

where q''_{rad} (W m^{-2}) is the boundary radiation heat flux, ε is the cell surface emissivity, and σ (W m^{-2} K^{-4}) is the Stefan-Boltzmann constant. The current implementation of the thermal abuse model considers the SEI decomposition, negative lithium-solvent, positive active material-solvent, electrolyte decomposition, and electrolyte combustion reactions. The abuse model parameters used in this work are shown in

Table 4. The combustion reaction component is only taken into account if the conditions of the test and the cell configuration would typically lead to ignition of the gaseous electrolyte. The total heat generation associated with the abuse reactions is formed as a source term in the thermal energy equation and given as

$$Q_{gen} = Q_{sei} + Q_{ne} + Q_{pe} + Q_e \tag{11}$$

where the four right terms are the heat generated during the SEI decomposition, negative lithium-solvent reaction, positive active material-solvent reaction, and electrolyte decomposition, respectively, all in units of (W m^{-3}).

Table 3. Cell specifications and thermo-physical properties [33, 70].

Property	Positive Electrode			Separator	Negative Electrode			Electrolyte
	$LiCoO_2$	Al	PVDF	PP/PE/PP	Graphite	Copper	PVDF	$LiPF_6$/EC: DMC:EMC
ρ (kg m^{-3})	2500	1500	1750	492	2660	8900	1750	1290
c_p (J kg^{-1} K^{-1})	700	903	1120	1978	1437	385	1120	133.9
k (W m^{-1} K^{-1})	1.48	238	0.12	0.334	1.04	398	0.12	0.45

Table 4. Thermal abuse model parameters [20, 30, 32].

Parameter	Description	Value
A_{sei}	Frequency factor (s^{-1})	1.667×10^{15}
A_{ne}		2.5×10^{13}
A_{pe}		6.667×10^{13}
A_e		5.14×10^{25}
$E_{a,sei}$	Activation energy (J mol^{-1})	1.3508×10^5
$E_{a,ne}$		1.3508×10^5
$E_{a,pe}$		1.396×10^5
$E_{a,e}$		2.74×10^5
H_{sei}	Reaction heat (J kg^{-1})	2.57×10^5
H_{ne}		1.714×10^6
H_{pe}		3.14×10^5
H_e		1.55×10^5
c_{sei0}	Initial dimensionless content	0.15
c_{ne0}		0.75
α_0		0.04
c_{e0}		1
m_{sei}	Reaction order	1
m_{ne}		1
m_{pe1}		1
m_{pe2}		1
m_e		1
t_{sei0}	Initial SEI thickness	0.033
W_c	Material content (kg m^{-3})	1.39×10^3
W_p		1.3×10^3
W_e		5.0×10^3

Beginning at approximately 90 °C, the solid-electrolyte interphase layer can break down and release heat as it is in a meta-stable state. The rate of reaction for the SEI decomposition is given as

$$R_{sei} = A_{sei} \exp\left[-\frac{E_{a,sei}}{RT}\right] c_{sei}^{m_{sei}} \tag{12}$$

where R_{sei} (s^{-1}) is the SEI reaction rate, A_{sei} (s^{-1}) is the SEI decomposition frequency factor, $E_{a,sei}$ $(\mathrm{J\,mol}^{-1})$ is the reaction activation energy, R $(\mathrm{J\,mol}^{-1}\,\mathrm{K}^{-1})$ is the gas constant, T (K) is the local cell temperature, c_{sei} is the dimensionless concentration of meta-stable species containing lithium in the SEI layer, and m_{sei} is the reaction order. The heat generated and the change in reacting species content during this reaction is given as

$$Q_{sei} = H_{sei} W_c R_{sei} \tag{13}$$

$$\frac{dc_{sei}}{dt} = -R_{sei} \tag{14}$$

where Q_{sei} $(\mathrm{W\,m}^{-3})$ is the volumetric heat generation, H_{sei} $(\mathrm{J\,kg}^{-1})$ is the specific heat release, and W_c $(\mathrm{kg\,m}^{-3})$ is the carbon content per volume.

Next in the reaction sequence is the reaction between intercalated lithium in the anode and the electrolyte, effectively forming a second SEI layer beginning at approximately 120 °C. The rate of the negative-solvent reaction is given as

$$R_{ne} = A_{ne} \exp\left[-\frac{t_{sei}}{t_{sei,ref}}\right] c_{ne}^{m_{ne}} \exp\left[-\frac{E_{a,ne}}{RT}\right] \tag{15}$$

where R_{ne} (s^{-1}) is the reaction rate, A_{ne} (s^{-1}) is the frequency factor, t_{sei} is the SEI thickness, $E_{a,ne}$ $(\mathrm{J\,mol}^{-1})$ is the reaction activation energy, c_{ne} is the dimensionless

concentration of lithium in the anode, and m_{ne} is the reaction order. The heat generated and the change in reacting species content during this reaction is given as

$$Q_{ne} = H_{ne} W_c R_{ne} \tag{16}$$

$$\frac{dt_{sei}}{dt} = R_{ne} \tag{17}$$

$$\frac{dc_{ne}}{dt} = -R_{ne} \tag{18}$$

where Q_{ne} ($\mathrm{W\,m^{-3}}$) is the volumetric heat generation, and H_{ne} ($\mathrm{J\,kg^{-1}}$) is the specific heat release.

The reaction between the cathode active material and the electrolyte begins to occur at 170 °C and is very exothermic. The heat released during the negative-solvent reaction can often be enough to initiate this reaction. The rate of the positive-solvent reaction is given as

$$R_{pe} = A_{pe} \alpha^{m_{pe}} \left(1-\alpha\right)^{m_{pe}} \exp\left[-\frac{E_{a,pe}}{RT}\right] \tag{19}$$

where R_{pe} ($\mathrm{s^{-1}}$) is the reaction rate, A_{pe} ($\mathrm{s^{-1}}$) is the frequency factor, α is the active material degree of conversion, m_{pe} is the reaction order, and $E_{a,pe}$ ($\mathrm{J\,mol^{-1}}$) is the reaction activation energy. The heat generated and the change in reacting species content during this reaction is given as

$$Q_{pe} = H_{pe} W_p R_{pe} \tag{20}$$

$$\frac{d\alpha}{dt} = -R_{pe} \tag{21}$$

where Q_{pe} (W m^{-3}) is the volumetric heat generation, H_{pe} (J kg^{-1}) is the specific heat release, and W_{pe} (kg m^{-3}) is the active material content per volume in the cathode.

The decomposition of the remaining electrolyte typically begins at 200 °C. The rate of the positive-solvent reaction is given as

$$R_e = A_e \exp\left[-\frac{E_{a,e}}{RT}\right] c_e^{m_e} \tag{22}$$

where R_e (s^{-1}) is the reaction rate, A_e (s^{-1}) is the frequency factor, $E_{a,e}$ (J mol^{-1}) is the reaction activation energy, c_e is the dimensionless concentration of the electrolyte, and m_e is the reaction order. The heat generated and the change in electrolyte concentration during this reaction is given as

$$Q_e = H_e W_e R_e \tag{23}$$

$$\frac{dc_e}{dt} = -R_e \tag{24}$$

where Q_e (W m^{-3}) is the volumetric heat generation, H_e (J kg^{-1}) is the specific heat release, and W_e (kg m^{-3}) is the electrolyte content per volume. Electrolyte combustion is considered to be an additional heat released during the decomposition reaction and is accounted for by increasing the heat release for this reaction.

The thermal energy conservation equations are solved in the radial dimension with the appropriate boundary conditions using the finite difference method implemented in Battery Design Studio® [71]. The present simulations use a mesh size of 50 nodes and an adaptive time-step backward differencing scheme to accurately capture

the quick temperature rise during the thermal event in an efficient manner. The conventional oven test results were validated against experimental results from Hatchard et al. [30], as shown in Figure 3.

2.2 Experimental Method

Conventional oven test procedures consist of pre-heating an oven to the desired temperature and inserting the cell into the chamber at the start time. Some oven tests ramp the oven temperature slowly over time similar to the operation of an accelerated rate calorimeter. Once the desired temperature is achieved it is held constant before, during, and after a thermal event occurs. This ensures the complete reaction of the products in the cell. During the test, the cell can temperature is measured, typically on the surface, in one or more locations depending on the form factor of the cell. This test is well suited for the characterization of the abuse tolerance of a single cell.

The modified oven test is typically conducted in an enclosed chamber and consists of applying a thin, 2 inch square, constant power heater to the surface of a cell and monitoring the temperature response. This type of test is commonly used to test a multi-cell module for abuse tolerance as it is relatively inexpensive to perform since precise temperature control of the test article is not required. Figure 2 shows the cylindrical and prismatic spiral-wound cells with the heater installed before and after a modified oven test. During the test, the “trigger” cell is heated until a thermal runaway event occurs, and the damage to each neighboring cell is noted. The surface temperatures of the cells were monitored using K-type thermocouples, typically one per cell for multi-

cell tests. The cell temperatures, along with ambient temperature measured at least 8 inches from the test article, were sampled at a rate of 10 Hz for the duration of the tests.

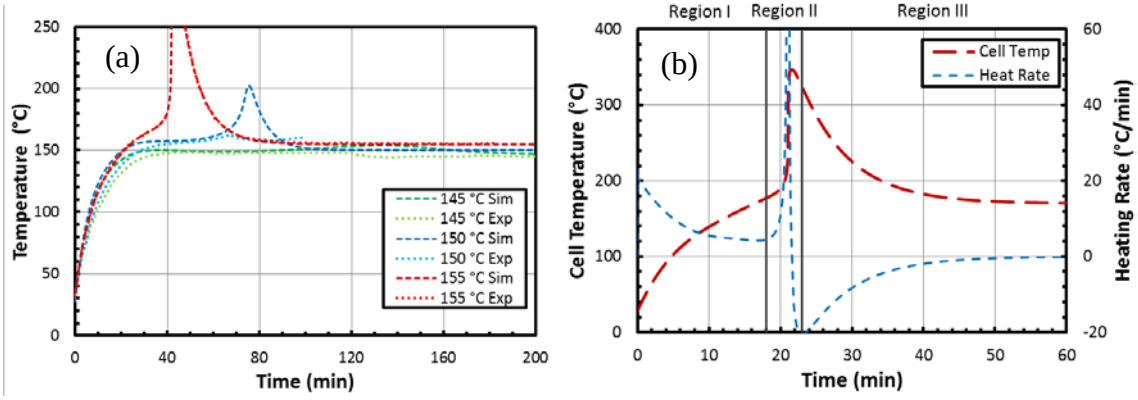

Figure 3. (a) Simulated and experimental cell temperature response for oven tests at 145, 150, and 155 °C for a lithium-cobalt-oxide 18650 cell. Results are in agreement with the work of Hatchard et al [30]. (b) Typical cell temperature and heating rate for 170 °C oven test of the same cell. The cell thermal behavior can be divided into three regions: initial heating (I), thermal event rapid heating (II), and final cooling (III).

For tests with the cells in a parallel electrical configuration, a single bank voltage is monitored during the test. The individual cell voltages and the series string voltage are monitored during the tests with serial test articles. Additionally, two cameras captured videos of the test from two angles, allowing for the identification of a thermal event. Numerous still images were taken before and after each test to document the test article configuration and post-test damage. All test articles in this work were pre-cycled with at

least two full charge-discharge sequences, and tested at 100% state-of charge. Lastly, the open circuit voltages (OCVs) of the tested cells were measured before the test to verify that they had been appropriately charged, and after the test to characterize the internal damage of the cell.

The cylindrical 18650 cells have vents located on the top of the cell that allows for an internal pressure release when the electrolyte vaporizes. However, the prismatic cell has two vents located on the flat side of the cell, which can shift the cell during the venting process. These side-facing vents can also be problematic in multi-cell modules, as the hot electrolyte vapors are pointed towards neighboring cells, facilitating the propagation of the thermal runaway condition. The cells were placed in a standing configuration to ensure that the cell vents were unobstructed for both form factors. For both cells, most tests induced venting, but only the prismatic cell demonstrated a sustained electrolyte flame, causing additional heat release.

The test procedure can be divided into three regimes. The first consists of heating a cell with a resistive heater supplied with constant power (constant current and voltage). This portion of the test reflects temperatures that are similar to that of a conventional oven test. The heater was supplied with 20 V and 1 A for all tests in this study for a power of 20 W. The second regime is where the majority of the reaction heat is released, and is generally referred to as when the “thermal event” occurs. The heater power is disabled once an event occurs. Cells often will vent gaseous electrolyte or rupture in this regime. Lastly, the final regime consists of the cooling of the cell back to environmental temperature. The temperature decay in this regime depends on the heat capacity of the

test articles, environmental conditions, and whether the electrolyte combusts. It is important to note that a nitrogen gas pre- and post-test purge was used due to its inert nature that prevented further cell reactions and improved test safety.

2.3 Results and Discussion

The thermal behavior of $LiCoO_2$ batteries of cylindrical and prismatic spiral-wound form factor is numerically simulated when subjected to both the standard oven abuse test and a constant-power heater test. The modified oven test is also conducted on the cells and the resulting thermal behavior is compared to the numerical results. The relative contribution of various exothermic side reactions is compared for the conventional and modified oven tests under various conditions and configurations. Additionally, the effect of convective heat transfer condition on the cell behavior when subjected to both tests is reported.

2.3.1 Effect of Oven Temperature

The simulated and experimental temperature responses of an 18650 cell at oven temperatures of 145, 150, and 155 °C are shown in Figure 3a adapted from the work of Hatchard et al. [30]. The surface heat transfer coefficient is taken to be 7.17 W/m^2K and the initial cell temperature is 28 °C. The simulated temperature during the 155 °C oven test shows a steady rise for the first 40 minutes, and then rapidly spikes in temperature to a maximum of 303 °C. This elevated temperature indicates that thermal runaway has occurred in this case. After the runaway event, the cell temperature decreases steadily to match the oven temperature where it remains for the remainder of the test. Next, the 150 °C oven test also shows a steady rise in temperature for the first 30 minutes. In

contrast, the temperature plateaus for about 40 minutes at 160 °C. At the 60 minute mark, the cell begins to heat further, peaking at 75 minutes with a temperature of 201 °C. The cell then cools back down to the 150 °C oven temperature. Lastly, for the 145 °C oven test, the cell heats steadily to a maximum temperature of 150 °C during the first 30 minutes, and the slowly decreases to the oven temperature of 145 °C. It can also be seen that the experimental results for the same oven temperatures are in agreement with the simulated results.

The temperature responses for the 145, 150, and 155 °C oven tests show that as the oven temperature increases, the onset of thermal runway occurs faster, and the severity of the runaway event increases as indicated by the higher peak temperature. It can be inferred from these results that onset of thermal runaway is characterized by an onset temperature. If a cell should reach and sustain that temperature, thermal runaway will certainly occur. It is shown that this temperature is between 145 and 150 °C for the cylindrical 18650 cell tested by Hatchard et al. [30]. Focusing on the most extreme case of a 155 °C oven, the steady initial rise in temperature shifts to a more accelerated rise around 25 minutes into the test. This is likely when the meta-stable component of the SEI layer in the anode decomposes and the lithium intercalated in the anode graphite reacts with the electrolyte solvent to form a new SEI layer. This reaction pushes the temperature well over the 155 °C oven temperature, triggering the positive-solvent and electrolyte decomposition reactions. The 150 °C oven test also induces temperatures beyond ambient, though in a more gradual manner so that the peak reaction is delayed by several minutes.

Using the validated model, the same cells were simulated with an oven temperature of 170 °C and h = 7.17 W/m^{2}K as depicted in Figure 3b. By calculating the heating rate of the cell from the slope of the temperature response, three thermal behavior regions can be seen. The first region (region I) is characterized by the initial heating of the cell by convection from the air in the elevated temperature oven. The heating rate starts at a maximum value of 20 °C/min as the temperature difference between the cell and the environment is the greatest at this point. This heating rate decreases steadily as the cell heats, the temperature difference decreases, and the heating via convection and radiation decreases. The heating rate then begins to stabilize and plateaus, still decreasing, as the internal heat generated from the SEI decomposition reaction begins. This reaction pushes the cell temperature just above the oven temperature, and initiates the negative-solvent reaction. The minimum heating rate value of 2 °C/min at 18 minutes into the test signals the end of region I. Region II begins with the aforementioned negative-solvent reaction which generates enough heat to reverse the trend of the cell heating rate from decreasing to increasing. At this time, the cell temperature is elevated enough to trigger the positive-solvent reaction, which in combination with the negative-solvent reaction, heats the cell to above 340 °C over a very short period of time. Once the reacting species is consumed, the cell no longer generates heat, and heat rejection from the cell to the surrounding oven cools the cell gradually down to 170 °C. Region II ends at the minimum value of heating rate, which represents the maximum cooling condition. This occurs at 23 minutes into this test. Region III is characterized by the cooling of the cell back to ambient conditions. The

slope of the temperature response and the magnitude of the heating rate is governed by the heat capacity of the cell, oven temperature, and assumed convection coefficient. The three regions of thermal behavior are referred to during the subsequent analysis. The results indicate that the severity and onset of thermal runaway are positive functions of temperature. A critical or "trigger" temperature can be defined as the temperature at which thermal runaway in eminent.

2.3.2 Effect of Convection Condition

It is clear from the results thus far the ambient cooling condition in the oven chamber, which is controlled by a circulation fan, affects the rate at which the cell temperature increases and decreases. Figure 4 shows the effect of four convection coefficients on the temperature response during conventional oven tests performed on an LCO 18650 cell at four oven temperatures. As shown previously, higher oven test temperatures result in an increase in probability and severity of a thermal event. While it was shown that there was a critical oven test temperature at which a cell would not go into thermal runaway, the results show that increasing the convective heat transfer coefficient also decreases the chance and severity of thermal runaway. For example, Figure 4a shows the temperature during oven tests at 145, 150, 155, and 160 °C at h = 5 W/m^2K. The peak cell temperature decreases with decreasing oven temperature, until the 145 °C test, where there is no noticeable peak in temperature, and therefore no thermal runaway event. This trend continues for the same oven tests conducted with an h = 10 W/m^2K, shown in Figure 4b. The 155 and 160 °C tests both went into thermal runaway,

but the 150 °C test only showed a minor peak in temperature that took nearly twice the time to reach than the warmer tests.

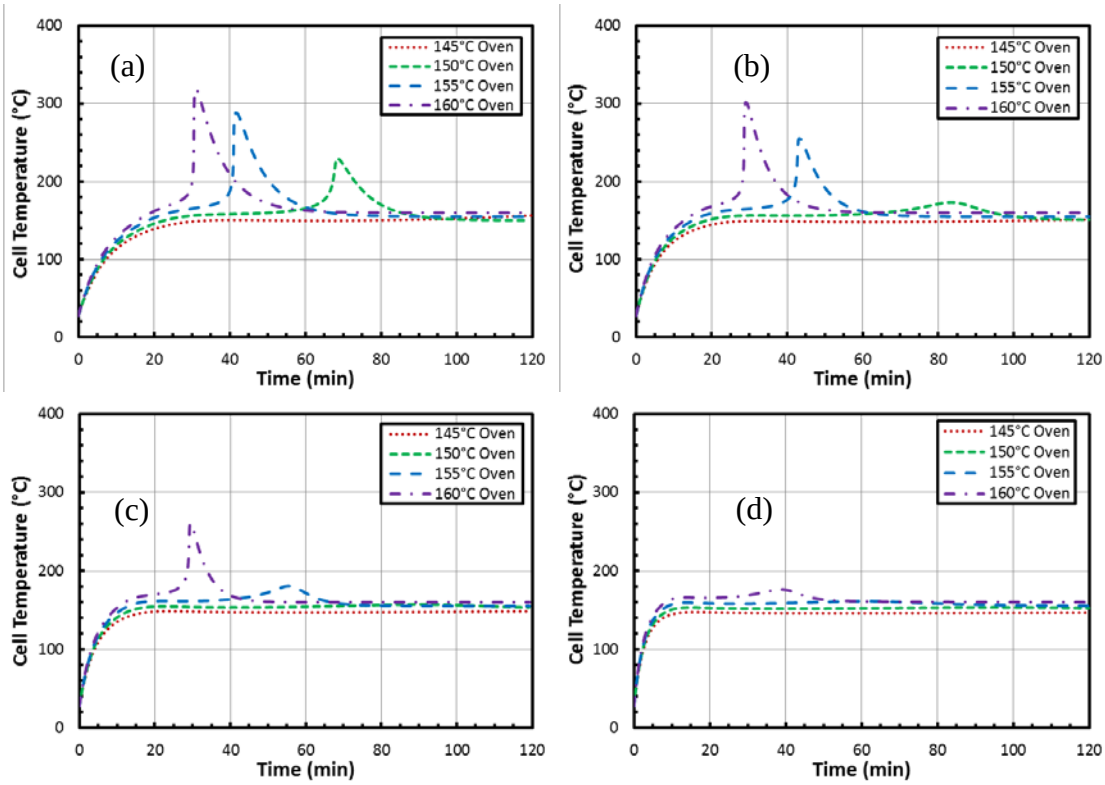

Figure 4. Temperature response for oven tests at 145, 150, 155, and 160 °C and environment convection coefficients of (a) 5, (b) 10, (c) 20, and (d) 40 W/m^{2}K.

This test also showed the lack of thermal runaway for 145 °C oven temperature. As shown in Figure 4c, increasing the convection coefficient to 20 W/m^{2}K decreases the temperature response for all cases and prevents thermal runaway for the 155 °C case, which had peak temperature of only 180 °C. Lastly, Figure 4d shows the test results for

h = 40 W/m^{2}K where none of the oven temperatures showed a temperature rise expected from a thermal runaway event. These results indicate that the critical temperature that triggers thermal runaway is affected by the convective heat transfer experienced by the cell. It is likely that this result translates to radiation heat transfer as well, where the surface emissivity affects the runaway onset temperature. The results that increasing convective heat transfer, leading to a faster rise in cell temperature and higher internal gradient, actually decreases the chances and severity of thermal runaway appear to be counterintuitive at first. However, the reason for this trend is that after the cell reaches the oven temperature, the heat generated from side-reactions is more easily dissipated to the oven environment. For most cases, this causes the heat generated during the SEI decomposition and negative-solvent reactions to be rejected to the oven before the next reactions in the chain can be triggered. This result indicates that cells in better contact with a cooling medium are less prone to thermal runaway even under abuse conditions. The importance of battery thermal management is not to be overlooked when considering abuse scenarios as a thermal runaway event caused by abuse may be prevented with sufficient cooling.

2.3.3 Influence of Abuse Reactions

To further elucidate the mechanisms of thermal runaway, the temperature evolution, heat rates, and concentrations of the reacting species are shown in Figure 5 for oven tests at 150 (test 1) and 170 °C (test 2) with h = 7.17 W/m^{2}K. These oven temperatures were chosen because one is characterized by severe thermal runaway and the other by the lack of a thermal event. Figure 5a shows the cell temperature and

heating rate for the two oven tests. During the initial heating in region I, the 170 °C test cell temperature rises faster, reaching 170 °C in about 16 minutes. The 150 °C test cell does not reach the oven temperature until 21 minutes into the test. This difference is further highlighted by the substantially higher heating rate for the 170 °C test, and can be explained by the dependence of convection heat transfer on the difference between the surface and ambient temperatures. This difference in initial heating rate affects the onset of the SEI decomposition, depicted by Figure 5b, which shows the amount of lithium containing meta-stable species in the SEI layer. Since the 170 °C test heats the cell faster, the SEI decomposes first for this test and over a shorter duration than the 150 °C case. Additionally, Figure 6 shows that the heat generated by the SEI decomposition reaction is 40% greater for the 170 °C test and is released in nearly half the time of the 150 °C reaction.

Several differences between the two tests are noted in region II, the event zone. First, the 170 °C test cell temperature begins to rise faster after reaching its oven temperature as indicated by the change in the heating rate trend from decreasing to increasing. The 150 °C test cell temperature rises beyond the oven temperature, but only by 5 °C. This subtle rise in temperature is caused by the negative-solvent reaction, depicted in Figure 5d, which shows the decrease in lithium intercalated in the anode as it reacts with the solvent. From 10 to 20 minutes, the anode lithium content for the 170 °C test steadily decreases until the thermal event when it plummets to its minimum value of 0.41. The negative lithium content for the 150 °C test only steadily decreases throughout the test and approaches a higher final value of 0.68. Since the cell temperature during the

150 °C test is much lower than that of the 170 °C test, the negative-solvent reaction occurs at a much lower rate delaying thermal runaway. This is further supported by the heat generation from the negative-solvent reaction, which rises and then tapers off to a relatively low value for the 150 °C oven test, but rises quickly and stays elevated for the 170 °C test.

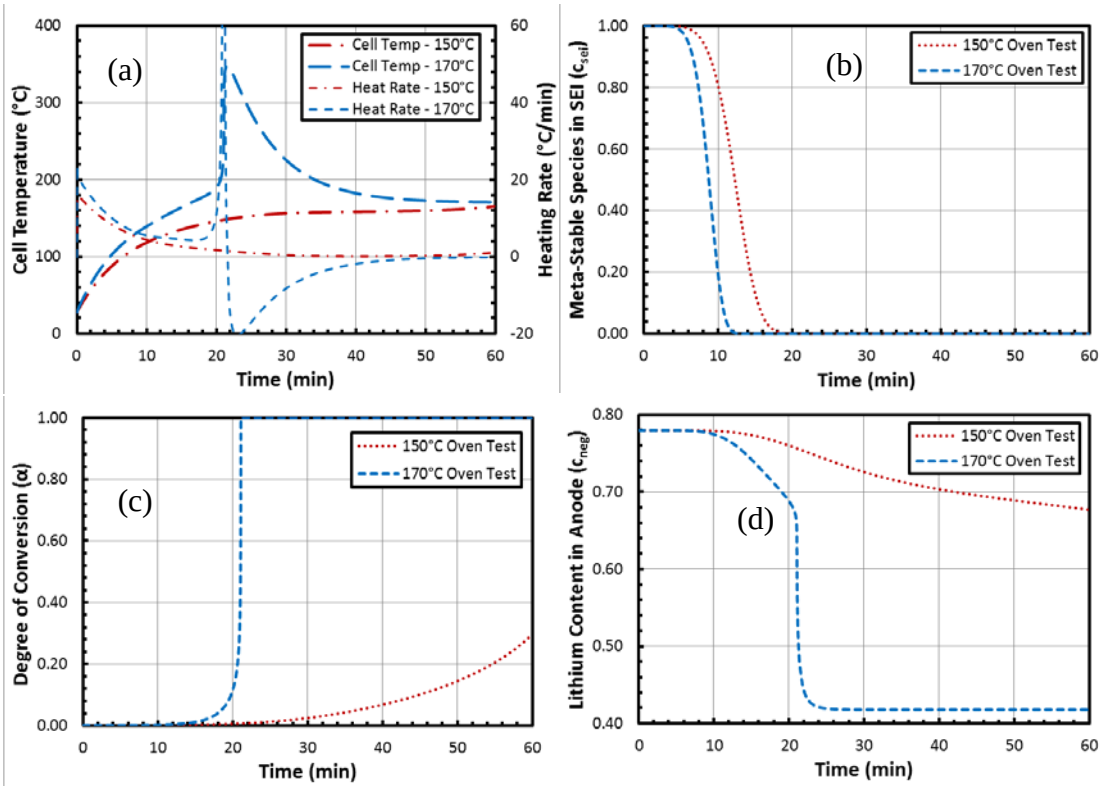

Figure 5. (a) Temperature and heating rate, (b) amount of meta-stable SEI, (c) cathode degree of conversion, and (d) anode lithium content during oven tests at 150 and 170 °C with a convection coefficient of 7.17 W/m^{2}K.

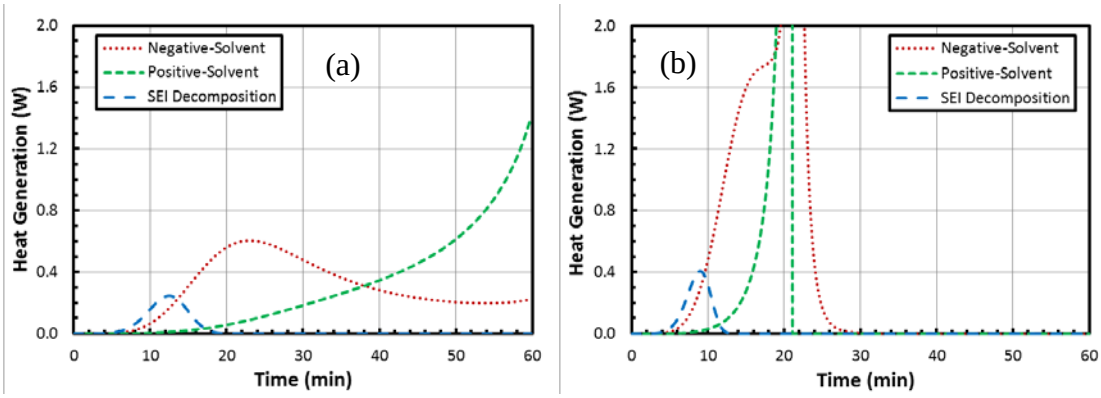

Figure 6. Heat generation for the SEI decomposition, negative-solvent reaction, and positive active material-solvent reaction during (a) 150 °C and (b) 170 °C oven tests.

Additionally, the 170 °C oven test conditions triggered the cell into thermal runaway while the 150 °C test cell was not triggered. This difference is influenced by combined effects of the positive and negative-solvent reactions, where the relevant species concentrations are shown in Figure 5c and 4d. The steady decrease in anode lithium content for the 150 °C test indicates that the negative reaction is sluggish, and the large drop in concentration for the 170 °C test indicates a quick reaction and a massive heat release leading to a thermal event. The heat released by the negative-solvent reaction directly affects the onset of the positive-solvent reaction. For example, the 150 °C oven test degree of conversion very slowly rises throughout the test, whereas the same for the 170 °C test rises very rapidly during the thermal event, and reaches unity at the time corresponding the to the peak cell temperature.

Lastly, during the cool-down phase, a slight increase in temperature of the 150 °C test indicates that the cell reaction is incomplete. In fact, the lithium content in the anode and cathode continues to decrease, and the heat generated by the positive-solvent reaction increases as the test continues. It is possible that should this cell be subjected to the elevated oven temperatures for a sufficiently long duration, it would go into thermal runaway. This indicates that the duration of exposure to thermal abuse conditions could also affect the onset of thermal runaway. Additionally, the results show that the heat generated from the SEI decomposition and negative-solvent reaction directly influences the onset of the positive-solvent reaction. Thermal runaway will certainly occur in the cell if the excess heat generated by these reactions is not dissipated quickly.

2.3.4 Modified Oven Test

The thermal responses of cells subjected to the constant power modified oven test are similar in nature to the responses under conventional oven test conditions. The behavior falls into the same three regions described previously: (I) pre-heating, (II) thermal event, and (III) cool down. Figure 7 shows the simulated and experimental thermal behavior of a cylindrical and prismatic spiral-wound cell subjected to the constant-power abuse test. The experimentally measured cylindrical cell response, shown in Figure 7a, is characterized by an initial heating stage, followed by a thermal event that has a peak temperature of over 500 °C. However, the simulated response of the same cell under the same conditions only estimates the peak event temperature to be 320 °C, a significant under-prediction.

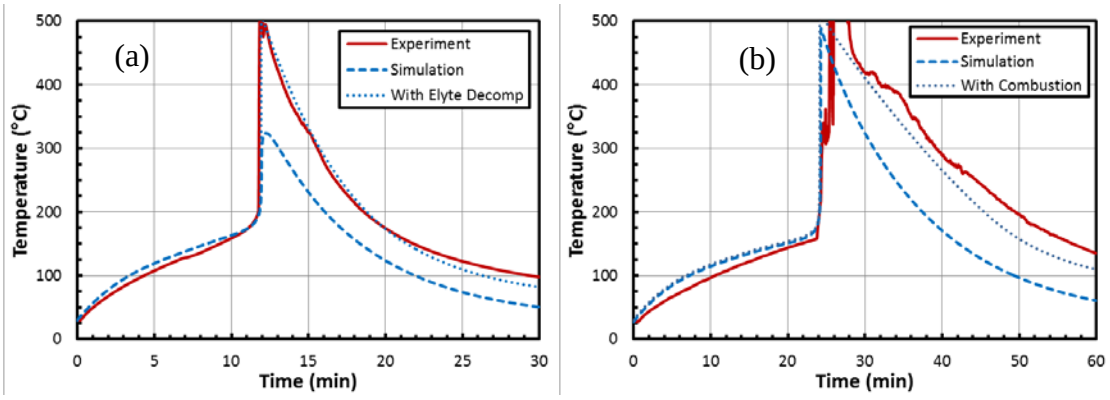

Figure 7. Temperature response during constant power abuse test and simulated oven test for (a) cylindrical and (b) prismatic spiral-wound cells. Note the contribution of the electrolyte decomposition and combustion reactions in these cases.

Furthermore, the simulated temperature in region III is consistently underestimated by the thermal abuse model. The reason for this difference is likely due to the model not accounting for the electrolyte decomposition reaction up to this point. By including this reaction in the thermal abuse model, a more accurate temperature curve is acquired that closely matches the experimental data.

A similar issue presents itself for the prismatic spiral-wound cell. The prismatic cell temperature during the test, shown in Figure 7b, is reasonably modeled until region III. The peak temperature of over 500 °C is captured well by the adjusted model that includes the electrolyte decomposition, but the temperature during the cool-down phase is again underestimated. The likely reason for this discrepancy is that during the experimental test for this cell, the unreacted electrolyte vented from the cell and ignited.

The additional heat released during this combustion is not typically accounted for in thermal abuse models and must be included to represent this test condition. This combustion heat is simply added as an additional source term in Equation 11. However, this generated heat may also affect the chamber temperature, so further analysis may be required to capture the residual heat entirely. In summary, to realistically capture the thermal behavior of these cells under a constant flux heating condition, modeling of the electrolyte decomposition and combustion is required.

2.3.5 Influence of Physical Configuration

The two form factors tested in this work demonstrated significantly different thermal behaviors. While the cylindrical cell heated, vented, and cooled in a predictable and consistent manner, the prismatic cell tended to be more active with rapid venting and electrolyte ignition. Aside from this difference, the prismatic cell also went into thermal runaway at 24 minutes into test compared to the cylindrical cell's trigger time of 12 minutes. This difference is due to the prismatic cell being nearly twice as massive as the cylindrical cell; 93.5 versus 50 grams. Additionally, the heat capacity of the cells is nearly the same due to the use of similar active materials. Therefore, the thermal mass of the prismatic cell is significantly greater than that of the cylindrical cell, yielding the slower rise in temperature. Because of this difference, the time scales are normalized when comparing the simulated results of these cells. Figure 8 shows the simulated temperature evolution and heating rate for both form factors when subjected to the modified oven test protocol. In the heating region, it is shown that the heating rate for

the cylindrical cell is more than double the heating rate for the prismatic cell, due to the aforementioned thermal mass difference.

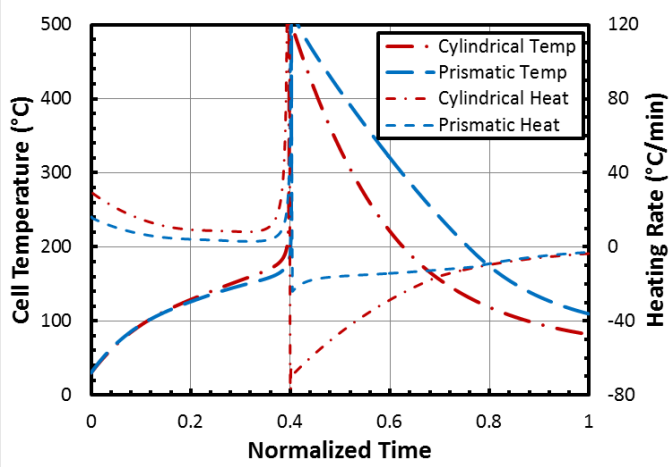

Figure 8. Temperature response and heating rate during simulated oven test for the cylindrical and prismatic spiral-wound cells.

The two cell temperatures in this region align almost exactly with each other on the normalized time scale until close to the onset of thermal runaway. The temperatures deviate when the SEI decomposition and negative-solvent reactions begin to occur. This is indicated by the reactant profiles shown in Figure 9 are nearly the same for both cases with some slight deviations in the SEI and anode lithium concentrations at the same time as the temperature deviation. The SEI decomposition reaction initiates for the prismatic cell first on the normalized time scale with the cylindrical occurring after. The same trend holds for the anode lithium content with the prismatic reacting first.

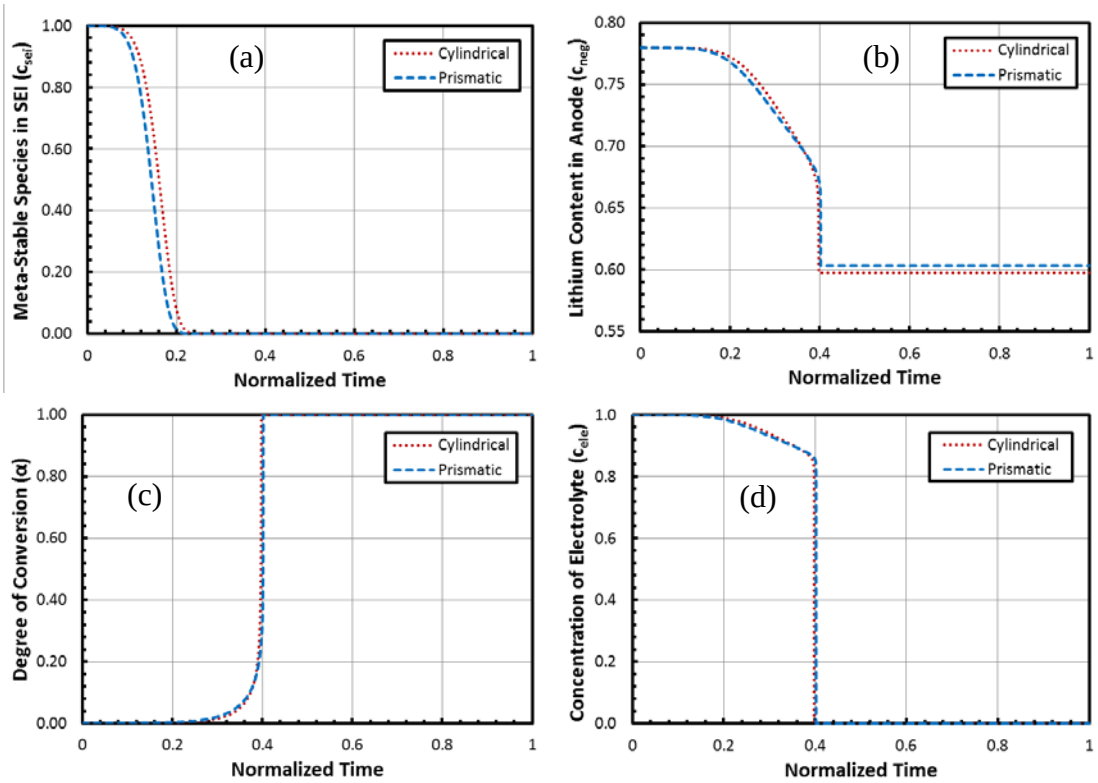

Figure 9. (a) Amount of meta-stable SEI, (b), cathode degree of conversion (c) anode lithium content, and (d) electrolyte concentration simulated oven test for the cylindrical and prismatic spiral-wound cells.

Additionally, Figure 10 shows that the SEI decomposition and negative-solvent reactions are lower in magnitude for the prismatic cell than that of the cylindrical cell. The slow reactions are also a product of the higher thermal mass associated with the prismatic cell. Since reactions are functions of temperature, reaction rates decreased with a slow temperature rise. Next, the onset temperature of prismatic cell is about 160 °C, which is lower than that of the cylindrical cell, which is about 190 °C. This is again due to the

difference in the thermal mass of the two cells, which also affects the positive-solvent and electrolyte decomposition reactions. Lastly, the difference in temperature response for the cool-down region is entirely due to the combustion of the electrolyte. These results indicate that an increased cell mass decreases the rate at which the temperature responds under thermal abuse conditions.

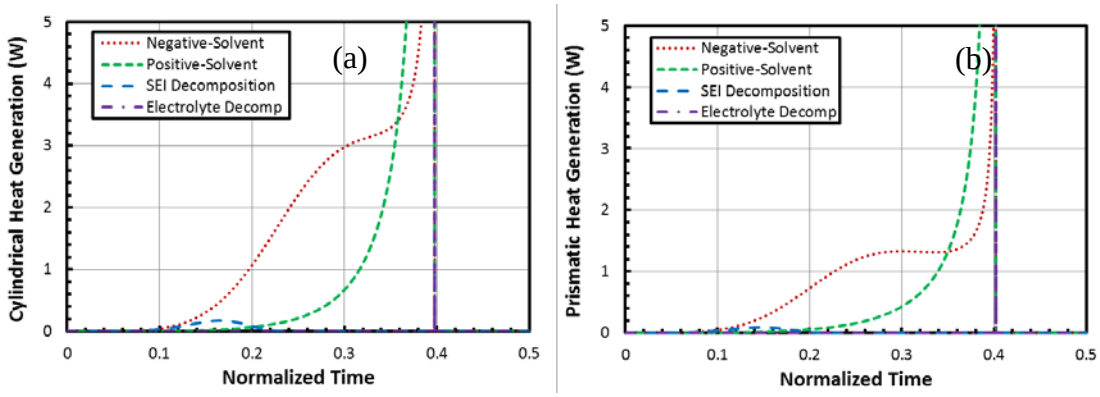

Figure 10. Heat generation for the SEI decomposition, negative-solvent reaction, and positive active material-solvent reaction, and electrolyte decomposition during simulated oven test for (a) cylindrical and (b) prismatic spiral-wound cells.

2.3.6 Effect of Convection for Modified Test

While the convection coefficient has been shown to have a significant effect on the thermal response during the conventional oven test, convection with the chamber could have a different effect for the modified oven test. Figure 11 shows the simulated temperature for the cylindrical cell at various convection conditions for the modified

oven test. For the initial heating region, it is shown that increasing the convective heat transfer coefficient decreases the temperature rise, which is contrary to the result for the conventional oven test shown in Figure 4. Additionally, the onset of thermal runaway and the peak temperatures of the cells are fairly consistent for the modified tests at the four convection conditions studied, which is different than the result from the conventional tests where increasing cooling condition decreased the chance and severity of thermal runaway. These results are because during the conventional test, convection is used to heat the cell from its initial temperature to the oven temperature, whereas in the modified test, convection works to dissipate the heat transferred to the cell via the flexible heater.

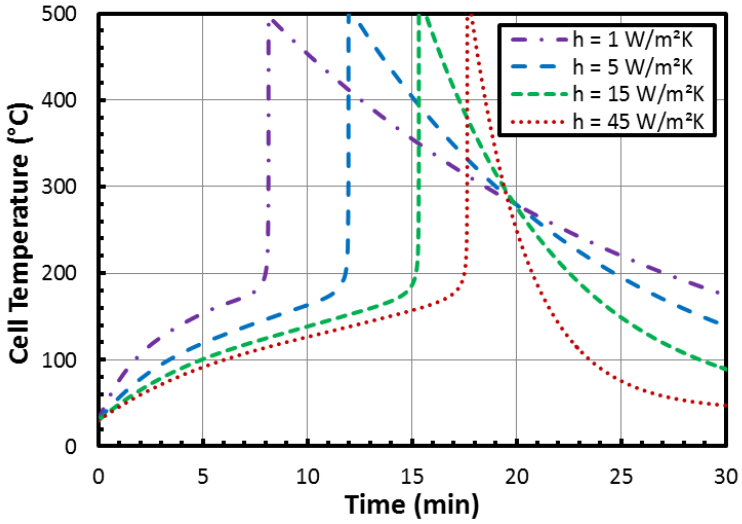

Figure 11. Simulated cell surface temperature for the cylindrical cell at 1, 5, 15, and 45 W/m^2K convective heat transfer coefficient under the modified oven test conditions.

Lastly, the decline in cell temperature during the cool-down phase is heavily dependent on the convection condition as low values of h induce a gradual decline and high values of h cause a rapid decline in temperature. Thermal gradients inside the cell could also play a role in abuse behavior. Thermal gradients are typically important when cells are of a large form factor since heat generated in the cell has to travel a greater distance before being dissipated. If the cooling condition is high at the surface and/or the cell is very thick, the cell core temperature could be many degrees hotter than the surface temperature, causing thermal runaway to occur sooner than anticipated. In summary, increasing the convection condition delays the onset of thermal runaway significantly, indicating that an adequate battery thermal management system could prevent the onset and propagation of thermal runaway.

2.4 Summary

In the present work a thermal abuse model is formulated to analyze the thermal runaway behavior of cells subjected to a constant heater power abuse test. This model was derived from conventional oven test protocol where a cell is subjected to a high temperature oven. The modified model was validated against experimental results for conventional oven tests and the effect of oven temperature and convection condition was determined. The probability and severity of thermal runaway increased with increased oven temperature and decreased convection coefficient for conventional oven tests. The abuse reaction sequence was identified as first SEI decomposition, then negative-solvent, and lastly positive-solvent for both the convention and modified oven tests. It was found that the electrolyte decomposition reaction must be included to accurately

model 18650 cells subjected to the modified test but was not necessarily required for the conventional test. Additionally, it was found that an electrolyte combustion reaction must be accounted for should the electrolyte ignite during the modified test. The simulated thermal behavior under constant-power heating condition was found to be in agreement with experiment. Next, the effect of the cell physical form factor was found for the modified test. The additional thermal mass of the prismatic cell caused slower temperature response and sluggish kinetics for the abuse reactions. Lastly, it was found that changing the convection condition had the opposite effect for modified test than what was found for the conventional test. This was due to the difference in the heating method between the two tests.

3. PROPAGATION OF THERMAL RUNAWAY

The objective of this section is to understand the effect of module configuration constraints such as cell spacing, tab style, cell form factor, and protection materials on the propagation of thermal runaway. An experimental approach is used to determine the thermal behavior of cells in close proximity to a cell that is subjected to constant flux heating.

The movement of the lithium ions and electrons generates heat via collisions with the various cell components, following Ohm's law. This generated heat is typically inconsequential and can be dissipated via a battery thermal management system with ease. However, at elevated temperatures, the reactivity of the electrode components increases exponentially by the Arrhenius equation [32]

$$R_i = A_i \exp\left(-\frac{E_a}{RT}\right) c_i^m \tag{25}$$

where R_i (s^{-1}) is the reaction rate, A_i (s^{-1}) is the reaction frequency factor, E_a (J mol^{-1}) is the reaction activation energy, R (J mol^{-1} K^{-1}) is the gas constant, T (K) is the local cell temperature, c_i is the concentration of the reacting species, and m is the reaction order. The reaction of the cell components is exothermic and can heat the cell further to activate additional side-reactions, leading to thermal runaway. Should a cell experience thermal runaway due to some abuse condition, the heat released from the reactions can cause neighboring cells to react. The rate at which heat is transferred from a triggered cell to another cell is influenced by the module design. For example, if a module is made

of 18650 cylindrical cells installed upright, the dominant methods of heat transfer are conduction through the tabs and the air between the cells. Applying Fourier's law of heat conduction to this system of two cells it can be said that [60]

$$Q_{cond,tabs} = k_{tab} A_c \frac{\left(T_1 - T_2\right)}{w} \tag{26}$$

where $Q_{cond,tabs}$ (W) is the heat transfer rate via conduction through the tabs, k_{tab} (W m^{-1} K^{-1}) is the tab thermal conductivity, A_c (m^2) is the tab cross-sectional area, T_1 (K) is the trigger cell temperature, T_2 (K) is the adjacent cell temperature, and w (m) is the length of the tab. To account for the heat transfer via conduction through the air, a shape factor approach can be used since the length of the cells is greater than the cell diameter and separation. For the two cylindrical cells,

$$Q_{cond,air} = S k_{air} \left(T_1 - T_2\right) \tag{27}$$

$$S = \frac{2\pi L}{\cosh^{-1}\left(\frac{4w^2 - D_1^2 - D_2^2}{2D_1 D_2}\right)} \tag{28}$$

where $Q_{cond,air}$ (W) is the heat transfer rate via conduction through the air, S (m) is the shape factor, k_{air} (W m^{-1} K^{-1}) is the air thermal conductivity, T_1 (K) is the trigger cell temperature, T_2 (K) is the adjacent cell temperature, L (m) is the cell length, and w (m) is the cell separation measured from the center axis, D_1 (m) is the diameter of cell 1, and D_2 (m) is the diameter of cell 2. These equations imply that the heat transfer rate is inversely proportional to the distance between the cells, so increasing cell spacing should reduce the chance of thermal runaway propagation and improve safety. However, during

thermal runaway cell temperatures can reach over 500 °C, and radiation becomes significant. Radiative heat transfer for a diffuse, grey body can be considered as

$$Q_{rad} = \frac{\sigma\left(T_1^4 - T_2^4\right)}{\frac{1-\varepsilon_1}{A_1\varepsilon_1} + \frac{1}{A_1 F_{12}} + \frac{1-\varepsilon_2}{A_2\varepsilon_2}} \tag{29}$$

where Q_{rad} (W) is the heat transfer rate via radiation, σ (W m^{-2} K^{-4}) is the Stefan-Boltzmann constant, $\varepsilon_{1,2}$ is the respective cell emissivity, and $A_{1,2}$ (m^2) is respective cell surface area [60]. F_{12} is the view factor for a system two cylinders of sufficient length given as

$$F_{12} = \frac{1}{2\pi}\left[\pi + \sqrt{C^2 - 4} - C - 2\cos^{-1}\left(2/C\right)\right] \tag{30}$$

$$C = 1 + \frac{\Delta x}{r} \tag{31}$$

where r (m) is the cell radius [60]. This shows definitively that increasing the cell spacing will decrease the rate of heat transfer via radiation. While it is more difficult to measure, electrolyte venting and ignition also influences the rate of heat transfer from a trigger cell to an adjacent cell. It is because of this difficulty that thermal runaway propagation testing is performed.

3.1 Propagation Abuse Test

The heat-to-vent, or artificial heating abuse test, can be performed either in an enclosed pressure vessel or on an open table, provided blast screens are used. A single cell in a multi-cell module is preinstalled with a thin 2 inch square Kapton® heating element designed to heat the cell to a temperature that initiates thermal runaway,

typically above 140 °C. Figure 2 shows the cells used in this study with the heater installed. The propagation of thermal runaway to neighboring cell is monitored by measuring the temperature of each cell using K-type thermocouples installed near the top of cells. Ambient temperature is also monitored via thermocouples throughout the test. At the start of the test, 20 V and 1 A is applied to the trigger cell using a regulated power supply for 20 W of heating. The heater power is shut off once the cell temperature spikes over 200 °C. Depending on the module configuration, either cell or bank voltages are monitored during the test, along with pre-and post-test open circuit voltages (OCV). Additionally, pictures and live videos are recorded from two angles during the tests. All data is sampled at a rate of 10 Hz to capture the rapid change in temperature during a thermal event. Lastly, for enclosed chamber tests, a nitrogen gas pre- and post-purge is used for test consistency and safety. Before the test, each test article was cycled at least twice according to the manufacturer charge specifications.

Two different cells were tested in this work. The first is a cylindrical spiral-wound 18650 cell, and the second is a prismatic spiral-wound cell. The specifications of each cell type are outlined in Table 5. The most notable differences between the two cells are that the prismatic cell is nearly twice the weight, volume, and capacity of the cylindrical cell. Additionally, the cylindrical cell has a vent located at the top of the cell that allows for an internal pressure release when the electrolyte vaporizes. However, the prismatic cell has two vents located on the flat side of the cell, which have been found to open more inconsistently than the cylindrical vents. These side-facing vents can also be problematic in multi-cell modules as the hot electrolyte vapors are pointed towards

neighboring cells, propagating the thermal runaway condition. The cells were assembled into test articles by resistance welding thin nickel tabs to the terminals of the cells. The various test article configurations are outlined in Table 6. The test articles consisted of either four or nine cells in series or parallel depending on the test and had various cell spacing. The electrical configuration naming convention is the number of cells followed by a P or S for parallel or series, and the cell manufacturer. Additionally, the tab configuration was varied with the M-style tabs being a branched approach and the S-type a serpentine approach. For the nine-cell modules, the center cell, cell 5, was artificially heated using the thin-film heater, shown installed on the cylindrical cell in Figure 2a. Figure 2b shows the heater installed on the prismatic cell. For the four-cell modules, the corner cell, cell 2, was forced into thermal runaway.

Table 5. Cell specifications and recommended operating conditions.

Model	Cylindrical	Prismatic
Capacity (Ah)	2.8	5.3
Max Voltage (V)	4.35	4.2
Min Voltage (V)	3.0	2.75
Max Discharge (A)	4.05	13
Max Charge (A)	2.7	10.6
Dimensions (mm)	18 x 18 x 65	19 x 64.8 x 37.3
Mass (g)	47.0	93.5
Discharge Temp (°C)	-20 to 60	-40 to 70
Charge Temperature (°C)	0 to 45	-20 to 60
Vent Location	Top (1 vent)	Side (2 vents)

Table 6. Test article specifications and general test plan.

Cell	Electrical	Tab	Spacing	SOC	Material	Result
Cylindrical	9P	M-type	1 mm	100%	None	Figure 12
Cylindrical	9P	M-type	2 mm	100%	None	Figure 13
Cylindrical	9P	M-type	4 mm	100%	None	Figure 14
Cylindrical	9P	S-type	1 mm	100%	None	Figure 15
Cylindrical	9P	S-type	2 mm	100%	None	Figure 16
Prismatic	9S	Alternating	2 mm	100%	None	Figure 17
Prismatic	4P	M-type	8 mm	100%	Radiant Barrier	Figure 18
Prismatic	4P	M-type	8 mm	50%	Radiant Barrier	Figure 19
Prismatic	9P	M-type	5 mm	50%	Intumescent	Figure 20

To decrease the chance of thermal runaway propagation of the prismatic cells insulation materials were installed between the cells because of their side-facing vents. The first material is a radiant barrier, which consists of a heat-resistant fiber material sandwiching multiple layers of highly reflective metal foil. This barrier is designed to block the electrolyte vapors and flame, which severely limits the radiation heat transfer by layering material. The next test material was a fire-resistant intumescent block that surrounds each cell. Intumescents are often used to give structural members in buildings up to 2 hours of fire resistance, tested by ASTM E119. The material transforms from a white thermoplastic into a dense, thermally insulating ash at approximately 200 °C. The heat released by a venting cell should activate this material, isolating it from neighboring cells.

3.2 Results and Discussion

The present work details the thermal runaway propagation behavior of the lithium-ion battery modules that were described previously. The cell temperatures during the constant-power heater test are reported along with cell and bank voltages when applicable. Open circuit voltages were recorded for each cell before and after the test. Photographs were taken after each test to characterize visible damage. In the subsequent analysis, physically adjacent cells are those that are direct north, south, east, or west of the trigger cell. Diagonal cells are those in the corners of the modules that are significantly further from the center due to the geometry of the modules. Electrically adjacent cells are those that are in direct contact with the trigger cell via tab connections. The onset of thermal runaway is characterized by temperatures above 200 °C, and a post-test OCV of 0 V.

3.2.1 Effect of Cell Spacing

Every test conducted on the 9P 18650 modules with M-type tabs released electrolyte vapor, but did not rupture, indicating that the vents worked as designed. In all cases, cells that were physically and electrically adjacent showed higher maximum temperatures and typically showed lower post-test OCVs. This indicates that electrical draining through the shorted trigger cell contributed significantly to the surrounding cell damage. However, none of the CYLINDRICAL tests showed thermal runaway propagation to neighboring cells indicated by sustained temperatures above 200 °C, likely due to either the resilient nature of the CYLINDRICAL cells or too slow of a

heating rate. However, there was obvious physical damage in most cases, and electrical draining was also apparent.

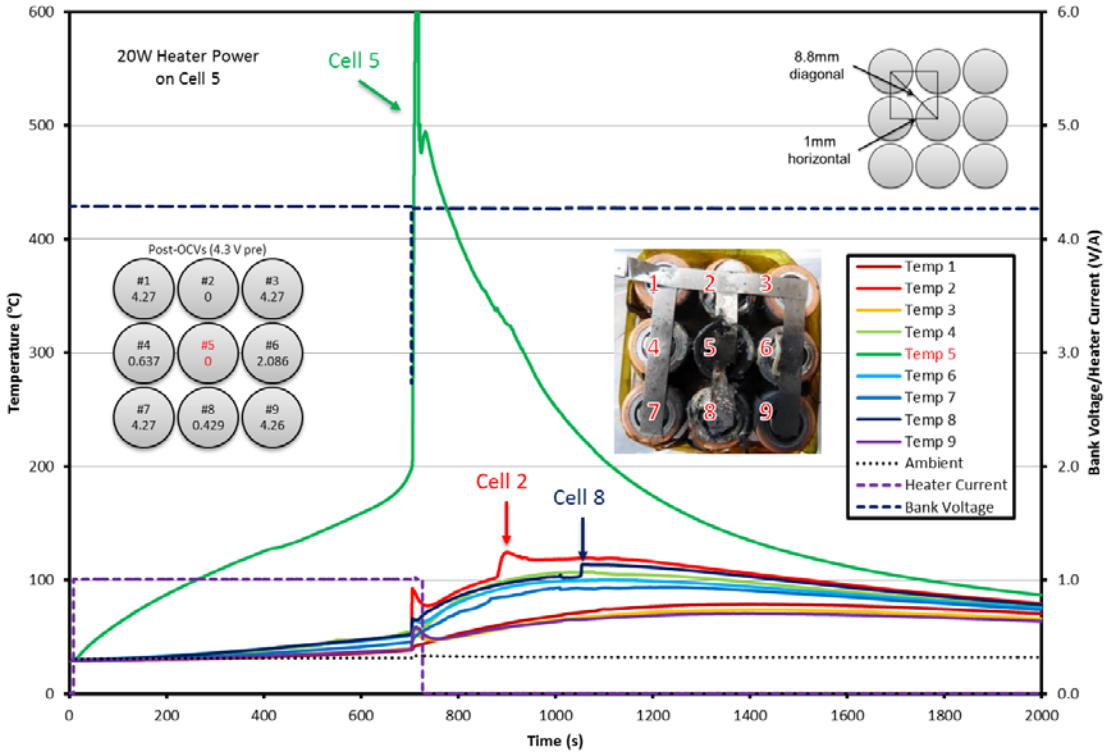

Figure 12. Measured temperature response of each cell in the tested module with heater current and bank voltage. Test article is a 9P 18650 with *M-type tabs*, *1 mm spacing*, 100% SOC, and no material between the cells. Cell 5 was artificially heated using constant power thin-film heating element.

For the 9P 18650 module with 1 mm spacing, the cells directly adjacent to the trigger cell showed significant damage in the form of charring from expelled electrolyte, as shown in Figure 12. Cells diagonal to the trigger cell showed significantly less visible

damage, with little charring or melting of the plastic wrapping. The tab at the trigger cell showed significant damage and was in fact completely burned off and disconnected. This was either due to the excessive resistive heating from high current loads through the tab due to the cell's short circuit, or due to the hot electrolyte vapors ejecting from the top of the cell. The post-test OCVs indicate that the adjacent cells sustained significantly more damage than the diagonal cells. The post-test OCVs of cells 1, 3, 7, and 9 were near the initial charge OCV of 4.3V. The adjacent cells 2, 4, 6, and 8 read 0, 0.6, 2.1, and 0.4 V, respectively. Maximum adjacent cell temperatures ranged from 100 to 125 °C (cells 6 and 2) and the maximum diagonal cell temperatures ranged from 70 to 93 °C (cells 9 and 7). The thermal runaway trigger temperature was 204 °C with a peak temperature of 665 °C.

Next, results of the test on the 9P 18650 module with 2 mm spacing are shown in Figure 13. Cells directly adjacent to the trigger cell showed less damage than that shown in the 1mm test. There was some charring from the expelled electrolyte but no melting of the plastic wrapping. Cells diagonal to the trigger cell showed significantly less visible damage with only slight charring. The tab at the trigger cell again showed significant damage and was completely burned off and disconnected. The post-test OCVs indicate that the adjacent cells sustained more damage than the diagonal cells. Cells 1, 3, 7, and 9 read OCVs near the charge OCV of 4.3V. The adjacent cells 2, 4, 6, and 8 read 2.1, 4.2, 2.56, and 0.187 V, respectively, considerably higher than the readings in the 1mm case. Maximum adjacent cell temperatures ranged from 88 to 104 °C (cells 4 and 8) and the maximum diagonal cell temperatures ranged from 58 to

69 °C (cells 7 and 3). Additionally, the thermal runaway trigger temperature was 186 °C with a peak temperature of over 600 °C.

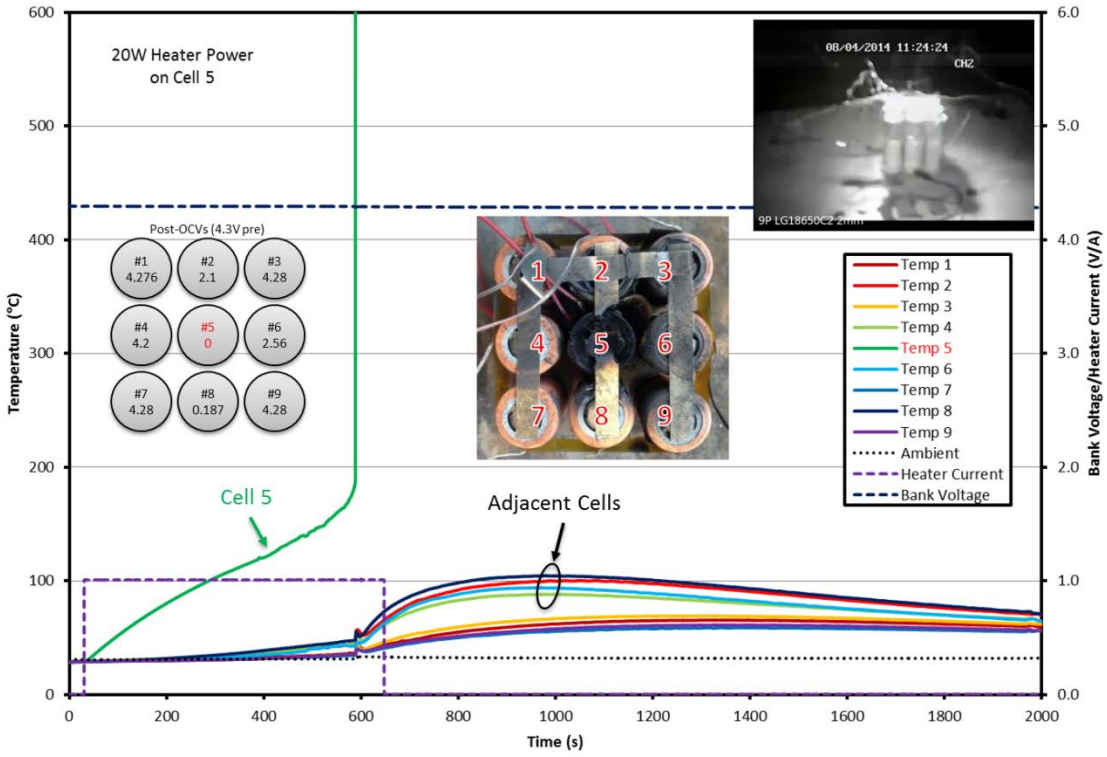

Figure 13. Measured temperature response of each cell in the tested module with heater current and bank voltage. Test article is a 9P 18650 with *M-type tabs, 2 mm spacing*, 100% SOC, and no material between the cells. Cell 5 was artificially heated using constant power thin-film heating element.

Lastly, the results for the 4 mm module are shown in Figure 14. The cells directly adjacent from the trigger cell showed little visible damage and the cells diagonal to the trigger cell showed no visible damage. Cells 1, 3, 5, 6, 7, and 9 read OCVs near the

charge OCV of 4.3V. The electrically adjacent cells 2 and 8 read 0.2 and 2.4 V, respectively, indicating considerable electrical draining. The maximum adjacent cell temperatures ranged from 78 to 102 °C (cells 6 and 2) and the maximum diagonal cell temperatures ranged from 56 to 64 °C (cells 7 and 1). Lastly, the trigger temperature was 189 °C with a peak temperature of 581 °C.

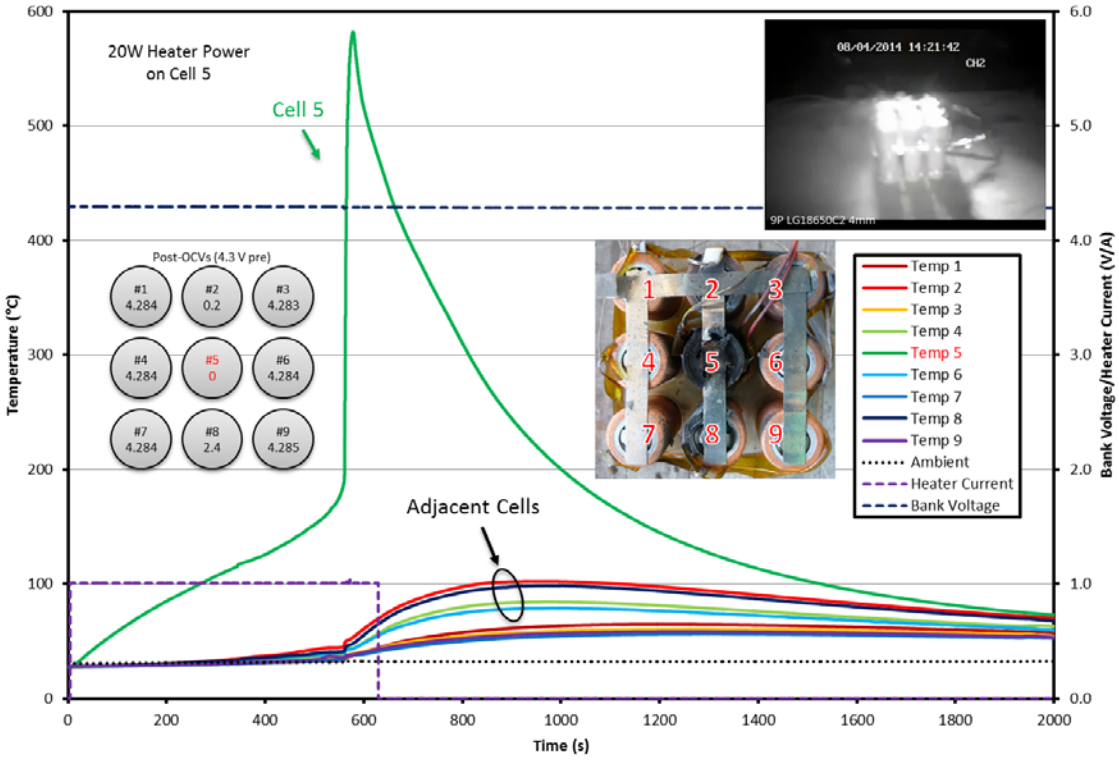

Figure 14. Measured temperature response of each cell in the tested module with heater current and bank voltage. Test article is a 9P 18650 with *M-type tabs, 4 mm spacing,* 100% SOC, and no material between the cells. Cell 5 was artificially heated using constant power thin-film heating element.

It is clear from the outcomes of these tests that increasing the cell spacing drastically decreases the damage sustained by the neighboring cells. Since the rate of heat transfer via radiation and conduction through the tabs decreases with increased distance, the increased spacing decreased the neighboring cell's temperature rise. The post-test voltages of the cells decreased due to both electrical draining through the shorted trigger cell and the positive temperature coefficient device that increases cell resistance with temperature. In general, a spacing of at least 2 mm is recommended for modules using 18650 cells due the drop in maximum adjacent temperature from 125 to 104 °C.

3.2.2 Effect of Electrical Configuration

The tests for the modules with M-type tabs indicate that electrical draining through the shorted trigger cell could have a significant effect on cell damage. The damage propagation is studied for modules with S-type tabs to compare with the M-type modules. The results of the test on the 9P 18650 module with 1mm spacing and S-type tabs are shown in Figure 15. The cells directly adjacent from the trigger cell showed significant damage in the form of charring and melting of the wrapping from expelled electrolyte. The cells diagonal to the trigger cell showed significantly less visible damage, with some charring or melting of the plastic wrapping, in a manner similar to the M-type test. In the S-type case however, the trigger cell tab was disconnected in 2 places and all post-test OCVs read 0 V. This indicates that the neighboring cells were

completely drained from the trigger cell short since they did not vent. Additionally, the maximum adjacent cell temperatures ranged from 115 to 146 °C (cells 2 and 4) and the maximum diagonal temperatures ranged from 88 and 95 °C (cells 3 and 7), significantly higher than the results from M-type test of the same spacing. Lastly, the trigger temperature was 119 °C with a peak temperature of 462 °C.

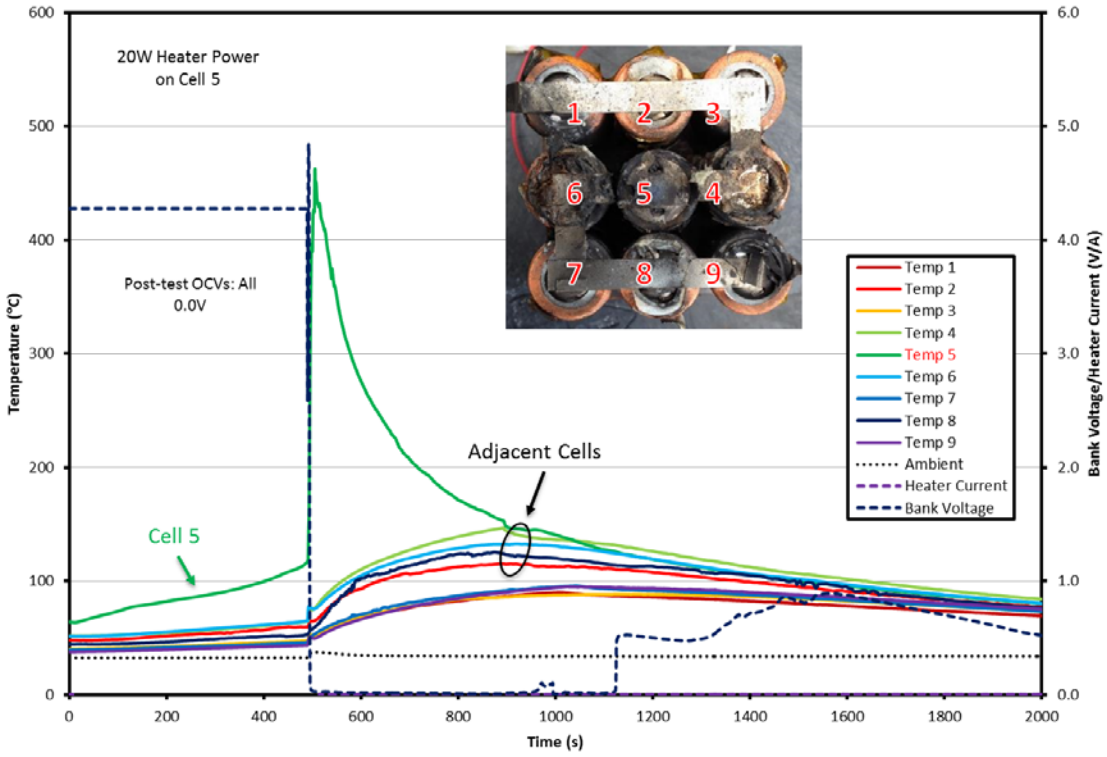

Figure 15. Measured temperature response of each cell in the tested module with heater current and bank voltage. Test article is a 9P 18650 with *S-type tabs, 1 mm spacing*, 100% SOC, and no material between the cells. Cell 5 was artificially heated using constant power thin-film heating element.

Next, the results of the test on the 9P 18650 module with 2 mm spacing and S-type tabs are shown in Figure 16. In this test, the cells adjacent to the trigger cell showed less damage than in the 1 mm test. There was some charring from the expelled electrolyte but no melting of the plastic wrapping with the exception of cell 4. In addition, cells diagonal to the trigger cell showed little damage, with only slight charring and the trigger cell tab was disconnected in two places. All post-test OCVs read 0 V again indicating that the cells were completely electrically drained. Maximum adjacent cell temperatures ranged from 92 to 125 °C (cells 8 and 4) and the maximum diagonal cell temperatures ranged from 59 to 87 °C (cells 7 and 1). The runaway onset temperature was 200 °C with a peak temperature of 639 °C

The modules with S-type tab configuration showed significantly worse behavior than the modules with M-type tabs under the same conditions. The S-type maximum adjacent cell temperatures were significantly higher with a 42 °C increase for the 1 mm modules and a 23 °C increase for the 2 mm modules when compared to the M-type tests. Additionally, the post-test OCVs for the S-type tests were consistently all zero voltages, in contrast with the M-type modules that showed some cells with voltage remaining after the test. This increase in maximum temperature and decrease in OCV indicates that the S-type tab configuration allows for more electrical draining into the trigger cell short than the M-type, which creates a safety concern. These results show that a branched style of tab configuration is safer than a serpentine style for modules with nine cells in parallel.

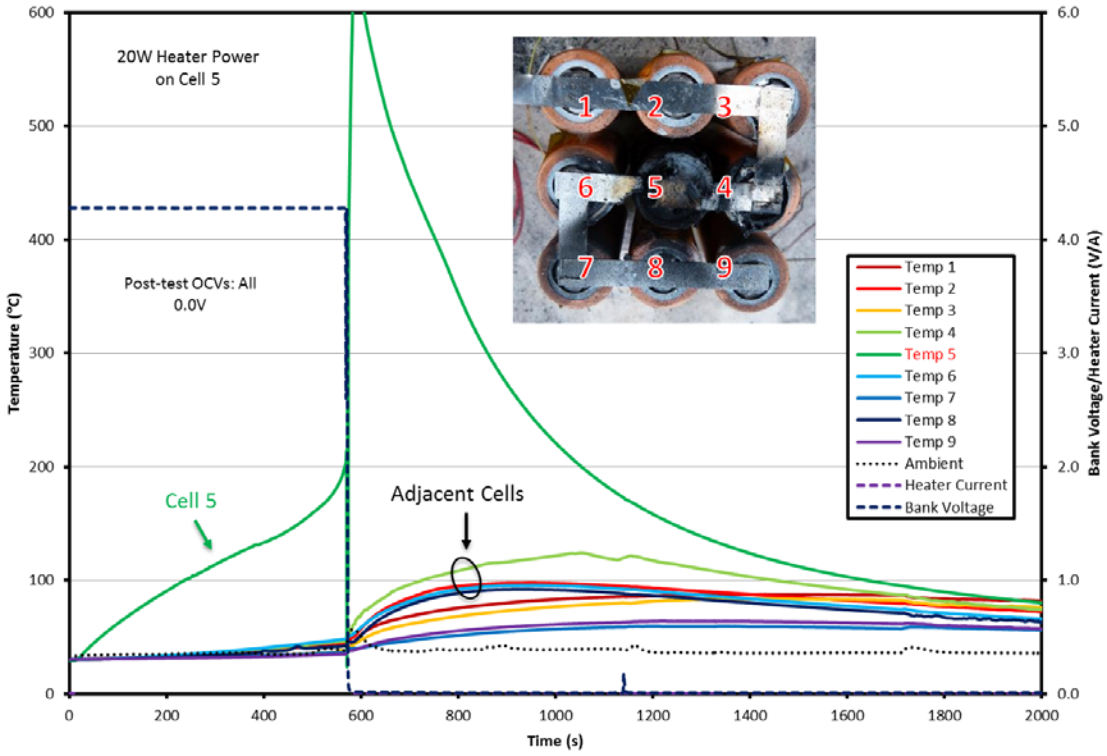

Figure 16. Measured temperature response of each cell in the tested module with heater current and bank voltage. Test article is a 9P 18650 with *S-type tabs*, *2 mm spacing*, 100% SOC, and no material between the cells. Cell 5 was artificially heated using constant power thin-film heating element.

3.2.3 Thermal Insulation Materials

Because the prismatic spiral-wound cells have side-facing vents, the thermal behavior of these cells under abuse is particularly interesting. Figure 17 shows the temperature response under 20 W of heater power applied to cell 5. During the first half of the test, cell 5 steadily increases in temperature to nearly 130 °C, with cell 8 also

heating to 80 °C due to its proximity to the heater. Half-way through the test, a release of electrolyte occurs and cells 2, 5, and 8 rapidly heat to over 600 °C. This indicates that the heat released during the thermal runaway of cell 5 significantly affects the neighboring cells when no inter-cell material is provided for protection. This runaway condition also propagates to cells 4 and 7. This result is supported by the drop in cell voltage corresponding to each cell's thermal runaway event. It is evident that simply spacing the prismatic cells away from each other will not sufficiently protect neighboring cells from a trigger cell due to the side facing vents. Installing thermal insulation materials between the cells to block the transfer of heat via the hot ejected electrolyte vapors could protect neighboring cells from thermal runaway damage.

The result of the 4P prismatic tests with the radiant barrier installed is shown in Figure 18. The trigger cell ejected its electrode and current collectors rapidly during the test. This indicates a rapid increase in internal pressure and failure of the vents to open to sufficiently release the electrolyte vapors in a controlled manner. The adjacent cells were relatively undamaged, with some dried electrolyte coated on the exterior and some swelling, but no evidence of venting or burned tabs. However, the adjacent cells all witnessed elevated temperatures for a short duration. Since temperature measurements are taken on the surface of the cells, the brief elevated temperatures are likely a consequence of quick exposure to the electrolyte vapors instead of sustained heating from thermal runaway. The post-test OCVs all read 4.2V with the exception of the trigger cell due to the ejection of the electrically active contents, causing the module to

be an open circuit. Lastly, the trigger temperature was 157 °C with a peak temperature of 496 °C.

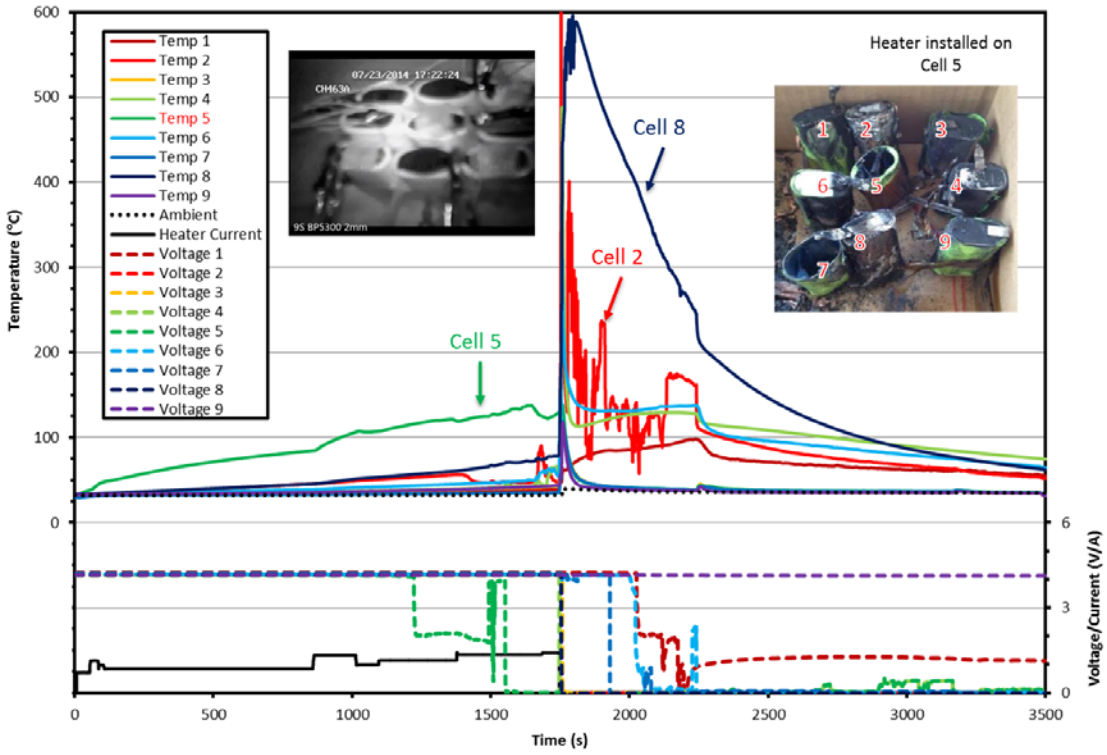

Figure 17. Measured temperature response of each cell in the tested module with individual cell voltage. Test article is a 9S prismatic with alternating tabs, 2 mm spacing, 100% SOC, and no material between the cells. Cell 5 was artificially heated using constant power thin-film heating element.

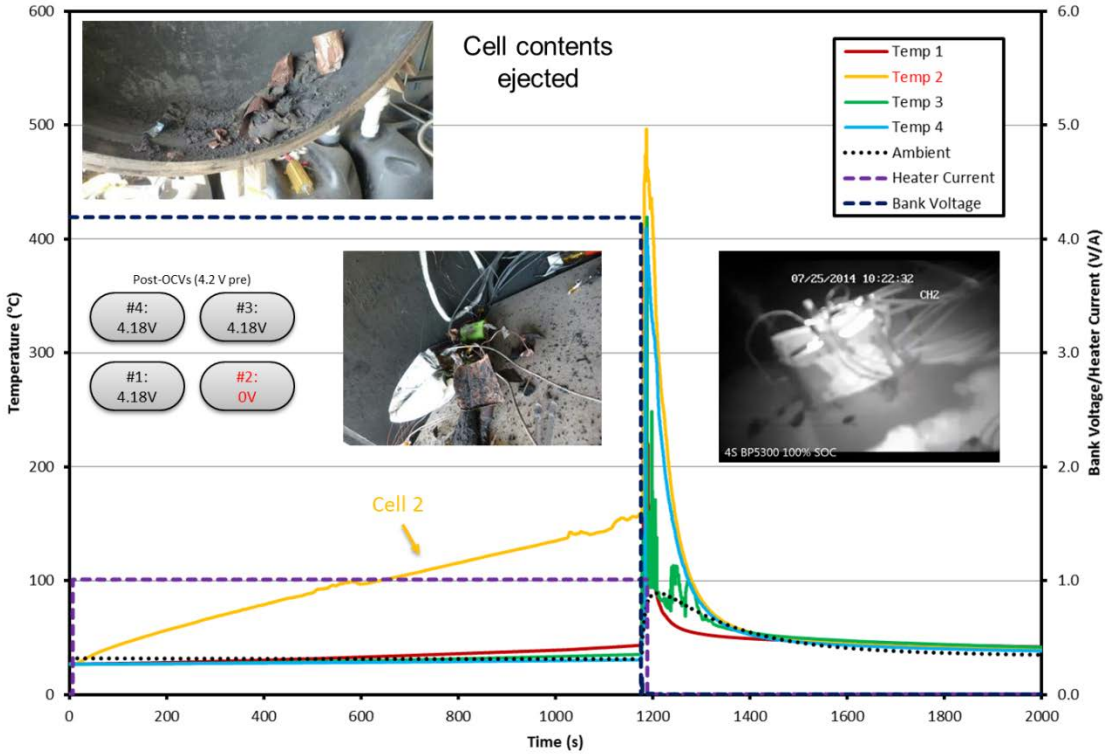

Figure 18. Measured temperature response of each cell in the tested module with individual cell voltage. Test article is a 4P prismatic with M-style tabs, 8 mm spacing, 100% SOC, and radiant barrier between the cells. Cell 2 was artificially heated using constant power thin-film heating element.

To test the effect of pre-test cell state-of-charge (SOC) on the thermal response, an identical test was conducted at 50% depth-of-discharge (DOD), and the results are shown in Figure 19. In this test, the trigger cell vents opened slowly and the electrolyte vapor ignited due to a spark generated by a melting tab at a temperature of 157 °C. The trigger cell temperature peaked at 700 °C and sustained a temperature of greater than

600 °C for several seconds during the fire, which appeared to be additionally fueled by the Kapton® tape used to secure the thermocouples.

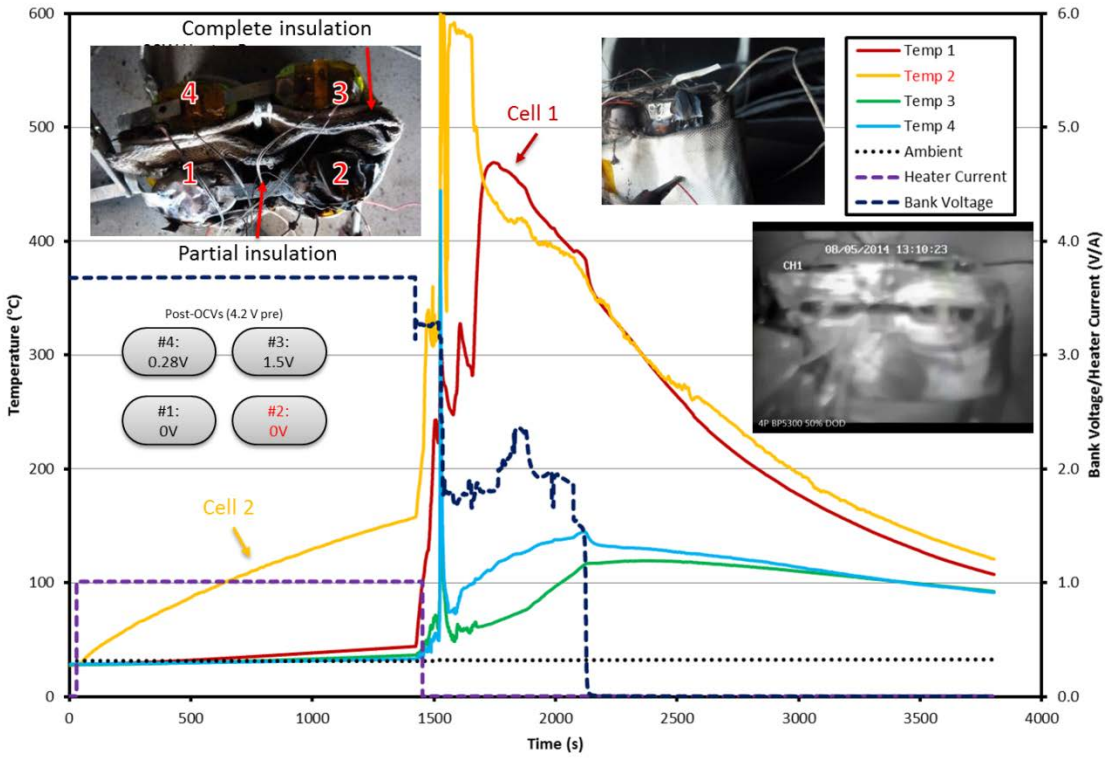

Figure 19. Measured temperature response of each cell in the tested module with individual cell voltage. Test article is a 4P prismatic with M-style tabs, 8 mm spacing, 50% SOC, and radiant barrier between the cells. Cell 2 was artificially heated using constant power thin-film heating element.

Due to the prolonged nature of this event, a significant amount of heat was generated and transferred from cell 2, the trigger cell, to cell 1, which is directly adjacent

to the trigger cell. Cell 1 showed significant damage in the form of charring and melted wrapping and appeared to have also vented slowly, but no flame was visible. Cells 3 and 4 were isolated from the trigger cell by the radiant barrier and showed some brief flash heating from the electrolyte flame, but did not sustain high temperatures. These cells did swell slightly, indicating vaporization of the electrolyte, but did not show a thermal event and did not vent electrolyte. With the exception of the quick spikes from the electrolyte fire, the protected cells' highest sustained temperatures were 119 and 144 °C for cells 3 and 4, respectively. The post-test OCVs were 0, 0, 1.5, and 0.28 V for cells 1 through 4, respectively. This agrees with the physical damage of the cells as cells 3 and 4 were relatively unharmed despite the electrolyte fire.

Next, the intumescent material was tested with a 9P prismatic module to determine its effectiveness at protecting cells adjacent to the abused cell. The pre- and post- test images are shown in Figure 20. Since the ends of the cell were held in place by the intumescent block lids, the cell was not allowed to rupture quickly and instead vented electrolyte that subsequently ignited. The electrolyte flame damaged the cells in close proximity to the trigger cell causing some charring and melting of the plastic wrapping. However, none of the other cells were visibly damaged. The maximum adjacent cell temperatures ranged from 106 to 416 °C (cells 8 and 4) and the maximum diagonal cell temperatures ranged from 75 to 164 °C (cells 7 and 3). The runaway onset temperature was 151 °C with a peak temperature of 735 °C. While the neighboring cell temperature appear to be higher for this test than for the radiant barrier cases, the high temperatures were not sustained for more than 10 seconds, indicating that the electrolyte

flame only rapidly heated the thermocouple, and was extinguished before the adjacent cells could go into thermal runaway. This is further supported by the post-test OCVs, which were all held at 3.76 V with the exception of the trigger cell, indicating that cells 4 and 6 were sufficiently protected by the intumescent material and only experienced quick heating from the flame.

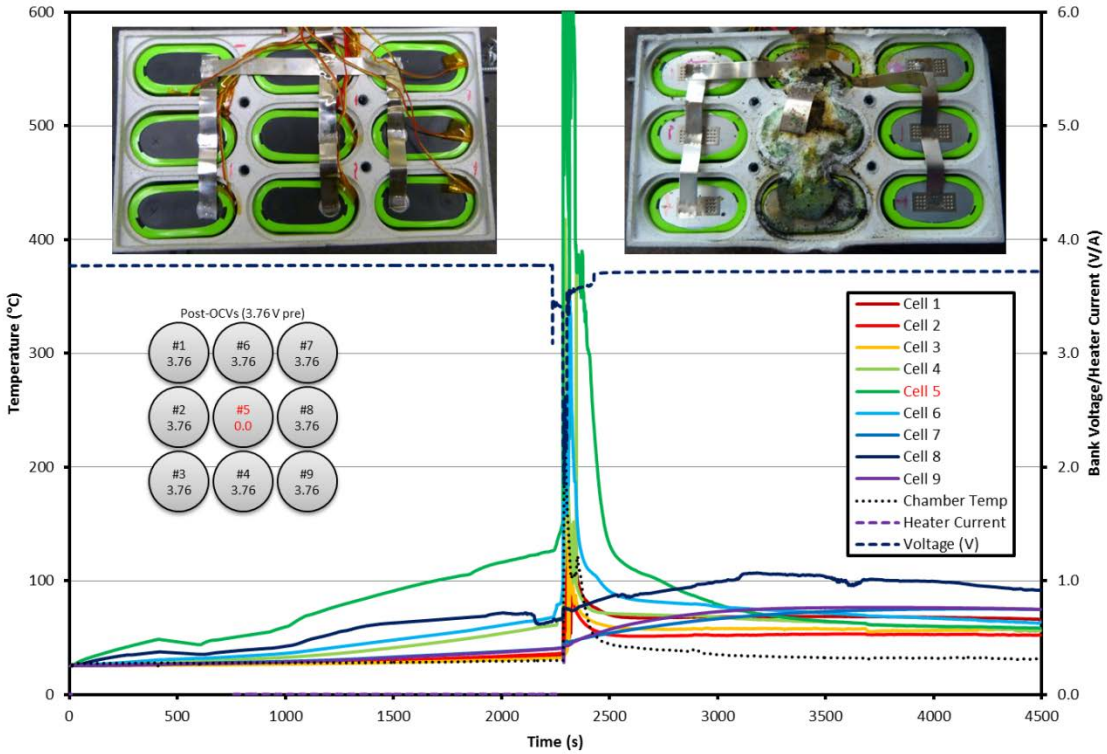

Figure 20. Measured temperature response of each cell in the tested module with individual cell voltage. Test article is a 9P prismatic with M-style tabs, 5 mm spacing, 50% SOC, and intumescent material between the cells. Cell 5 was artificially heated using constant power thin-film heating element.

In summary, it was shown that insulation materials can prevent the probable propagation of thermal runaway in modules constructed with the prismatic cells. The radiant barrier proved to sufficiently protect cells that were fully covered by the material. This barrier did not provide much rigidity to the module, however, as it allowed for the trigger cell to rapidly burst when charged to 100% SOC. Since the radiant barrier was not consumed during the thermal event, it could provide protection during sustained fire or venting. The relatively low density of the barrier also makes it desirable in applications where weight is critical. The intumescent material provided even more protection of the prismatic cells during thermal runaway. Unfortunately, the material's rapid change in volume due to intumescent reaction could prove to be problematic for some applications. Additionally, the material is considerably massive as it nearly doubled the weight of a nine cell module.

3.3 Summary

The influence of module design configurations including cell spacing, tabbing style, and vent location on thermal runaway propagation were analyzed experimentally in this work. It was found that increasing the distance between cells decreases the damage experienced by adjacent cells, decreases cell temperatures, and improves post-runaway voltages. Based on these results, a cell spacing of at least 2 mm is recommended to minimize the chance of thermal runaway propagation and module damage. Additionally, the tests showed that a branched style of tabbing improves the safety of the modules over a serpentine style of tabbing as the shorted trigger cell is electrically better isolated from the rest of the module when the tabs are branched. The vent location also significantly influenced runaway propagation, as the cells with side facing vents triggered propagation more often than the cells with top facing vents. To protect adjacent cells from electrolyte vapors released during venting, a radiant barrier and an intumescent material were installed between the cells with side-vents. Both insulation materials were able to protect surrounding cells from the heat released by the triggered cell. In conclusion, the proper method of minimizing the chance of thermal runaway propagation varies significantly with cell type and module configuration.

4. THERMAL MANAGEMENT

This section uses a coupled electrochemical-thermal numerical modeling approach to determine the effect of design considerations such as loading condition, PCM properties, inter-cell spacing, and material cap thickness on the maximum temperature and thermal gradient of a representative battery module containing a phase change material and actively chilled cold plates. The relative contribution of each constraint can be evaluated in combination with experimental data to improve future BTMS designs [72].

The cell of particular interest in this section is a cylindrical spiral wound 18650 cell, measuring 18 mm in diameter and 65 mm in height, with a capacity of 2.8 Ah, charge voltage of 4.3 V, and a cutoff voltage of 3.0 V. This cell uses a $LiCoO_2$ cathode, graphite anode, and $LiPF_6$/EC:EMC:DMC electrolyte. The module used in this simulation consists of a twenty-five cell aligned array organized in five series banks of five parallel cells each (5S5P). The cells are in thermal contact with the surrounding phase change material, which is in contact with cold plates on the top and bottom of the module. Figure 21 depicts the hybrid active/passive BTMS previously described. The heat generated within the cells is dissipated to the PCM and aluminum channel via conduction and finally heat is removed via convection from the coolant.

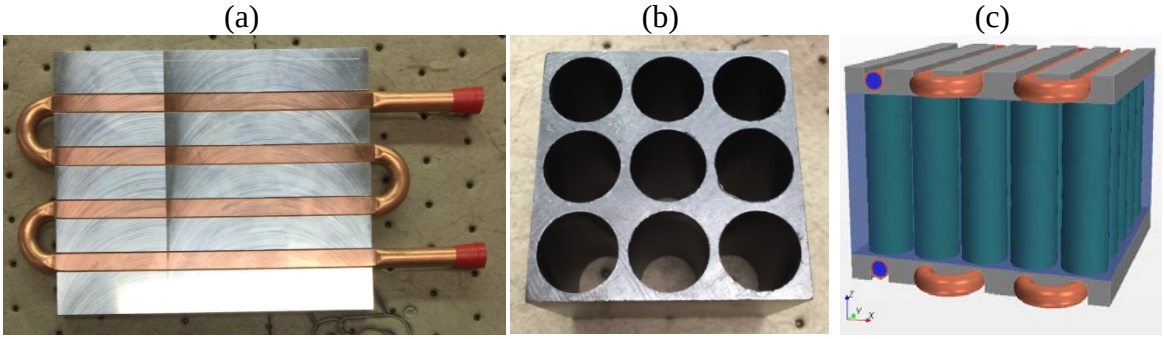

Figure 21. (a) Aluminum cold plate with inlaid copper tubing. (b) Paraffin wax phase change material block for a nine 18650 cell module. (c) Computational domain for the twenty-five cell module simulated in this study. Note phase change material denoted by the blue section surrounding the green 18650 cells. Two aluminum cold plates with inlaid copper tubing are installed on the top and bottom of the module.

4.1 Electrochemical-Thermal Model

The change in local temperature during cell discharge is found using numerical finite volume formulation implemented in STAR-CCM+® [73] to solve the thermal energy conservation equation in three dimensions given as

$$\rho c_p \frac{\partial T}{\partial t} = \nabla \cdot k \nabla T + Q_{gen} \tag{32}$$

where ρ (kg m^{-3}) is the cell density, c_p (J kg^{-1} K^{-1}) is the specific heat capacity of the cell, T (K) is the temperature, t (s) is time, k (W m^{-1} K^{-1}) is the cell thermal conductivity, and Q_{gen} (W m^{-3}) is the total heat generated by the cells during operation

[60]. The cell component thermo-physical properties are given in Table 3 and are used to calculate the cell bulk properties, which are assumed to be isotropic. The anisotropy of the cell thermal conductivity due to the layering of the internal components is taken account by

$$k_n = \frac{\sum_i l_i}{\sum_i l_i / k_i} \tag{33}$$

$$k_p = \frac{\sum_i k_i l_i}{\sum_i l_i} \tag{34}$$

where k_n (W m^{-1} K) is the normal direction thermal conductivity, k_p (W m^{-1} K) is the parallel direction thermal conductivity, l_i (m) is a layer's thickness, and k_i (W m^{-1} K) is a layer's thermal conductivity, taken from Table 3. Thermal contact resistance between the cells, PCM, and cold plate are considered. The contact resistance between the cells and cold plate is calculated based on a thin, electrically insulating thermal interface material to prevent shorting of the module series tabs.

The temperature field within the cells must be calculated in three dimensions, as the cell thermal gradients are of particular interest in this study. While a physics-based electrochemical model would be preferred for calculating cell temperature during discharge, these models are very computationally expensive [18]. Since we are interested in the effectiveness of the thermal management systems, the more efficient Newman, Tiedemann, and Gu (NTG) model based on empirical correlations is better suited [70, 74-76]. This model uses up to 6th order polynomial fits for open circuit voltage and cell

impedance as functions of depth of charge and temperature. This allows for the temperature of the cell to be calculated as a function of the voltage and depth of charge at each computational cell. Equations 4 through 8 detail the NTG electrochemical model.

$$V_{cell}\left(DoD, J\right) = -\frac{J}{Y} + U + c\left(T - T_{ref}\right) \tag{35}$$

$$DoD = \frac{\int Idt}{C}, J = \frac{I}{A_s} \tag{36}$$

$$U = a_0 + a_1 DoD + a_2 DoD^2 + a_3 DoD^3 \tag{37}$$

$$Y = \left\{b_0 + b_1 DoD + b_2 DoD^2 + b_3 DoD^3\right\} \exp\left(\frac{E_a}{R}\left(\frac{1}{T_{ref}} - \frac{1}{T}\right)\right) \tag{38}$$

$$Q = I \cdot \left(U - V_{cell} - T\frac{dU}{dT}\right) \tag{39}$$

where V_{cell} (V) is the closed circuit voltage, J (A m^{-2}) is the current density, Y (S m^{-2}) is the conductance, U (V) is the equilibrium voltage, c (V K^{-1}) is the voltage-temperature correction coefficient, T (K) is the local temperature, T_{ref} (K) is the reference temperature, DoD is the depth of discharge, I (A) is the current, C (Ah) is the cell capacity, A_s (m^2) is the electrode surface area, E_a (J mol^{-1} K^{-1}) is the activation energy, R (J mol^{-1}) is the gas constant, Q (W) is the local heat generation, $a_{0,1,2,3}$ (V) are the equilibrium voltage fit coefficients, and $b_{0,1,2,3}$ (S m^{-2}) are the conductance fit coefficients. Table 7 details the parameters required for this model. This electrochemical model is implemented by Battery Design Studio® [71] and combined

with the thermal and flow solvers in STAR-CCM+® to develop the coupled thermal-electrochemical solution set.

Table 7. Electrochemical-thermal model parameters [70].

Parameter	Value	Units
a_0	4.1638	V
a_1	-2.5926	V
a_2	4.6004	V
a_3	-2.9808	V
b_1	877.368	S m^{-2}
b_2	-477.686	S m^{-2}
b_3	128.683	S m^{-2}
c	$9.5x10^{-4}$	V/K
E_a	15000	J/mol
T_{ref}	298.15	K

4.2 Management System Model

It is important to capture the effects of the phase change material's latent heat when solving the energy equations in 3D. Therefore, a coupled multi-phase model must be included in the simulation to show the local effect of heat absorption by the PCM. The Euclidian multi-phase volume of fluid (VOF) model is best suited for flows in which each phase constitutes a large structure and the interphase contact area is relatively small, both of which are true in this simulation [77, 78]. In this model, the spatial distribution of each phase is simply given as a volume fraction. The flow and thermal equations are solved for an equivalent fluid with thermo-physical properties that are functions of each phase's properties. The formulation is given as

$$\rho = \sum_i \rho_i \alpha_i \tag{40}$$

$$\mu = \sum_i \mu_i \alpha_i \tag{41}$$

$$c_p = \sum_i \frac{c_{pi}\rho_i}{\rho} \alpha_i \tag{42}$$

$$\alpha_i = \frac{V_i}{V} \tag{43}$$

where ρ ($\mathrm{kg\ m^{-3}}$) is the total density, μ ($\mathrm{Pa\ s}$) is the total viscosity, c_p ($\mathrm{J\ kg^{-1}\ K^{-1}}$) is the total specific heat capacity of the cell, V ($\mathrm{m^3}$) is the total volume, and α_i is the phase volume fraction. The subscript i denotes the property of the i^{th} phase in a multiphase region. These properties are then used in combination with the regional velocity field to solve the phase mass conservation equation

$$\frac{d}{dt}\int_V \alpha_i dV + \int_S \alpha_i \left(v - v_g\right) \cdot dA = \int_V \left(s_{\alpha_i} - \frac{\alpha_i}{\rho_i}\frac{D\rho_i}{Dt} \right) dV \tag{44}$$

where v ($\mathrm{m\ s^{-1}}$) is the local velocity, v_g ($\mathrm{m\ s^{-1}}$) is the bulk region velocity, and s_{α_i} is a phase source term. Since the phase change materials studied in this work are encapsulated in a rigid expanded graphite structure, the velocity in the phase change region can be considered to be zero for both the solid and liquid phases and the convection and source terms drop out of Equation 8. To capture the temperature field and solid volume fraction in the phase change material, a melting-solidification model is required [79]. The model uses in this work is based on an enthalpy approach to determine the distribution of solid phase in a surrounding liquid phase. The melting-solidification model is given by

$$h_{ls} = h_s + \left(1 - \alpha_s\right) h_{latent} \tag{45}$$

$$\alpha_s = \begin{cases} 1 & \text{if} \quad T' < 0 \\ f\left(T'\right) & \text{if} \quad 0 < T' < 1 \\ 0 & \text{if} \quad 1 < T' \end{cases} \tag{46}$$

$$T' = \frac{T - T_{sol}}{T_{liq} - T_{sol}} \tag{47}$$

$$f\left(T'\right) = 1 - T' \tag{48}$$

where h_{ls} (J kg^{-1}) is the liquid-solid enthalpy, h_s (J kg^{-1}) is the sensible heat, α_s is the solid phase volume fraction, h_{latent} (J kg^{-1}) is the latent heat of fusion, T' is a normalized transition temperature, T (K) is the local temperature, T_{sol} (K) is the solidus temperature, T_{liq} (K) is the liquidus temperature, and $f\left(T'\right)$ is the solid fraction function that establishes the dependence of solid volume fraction on temperature [80-82]. Since the phase change materials in this work are not pure, the liquidus and solidus temperatures differ by a few degrees, and the latent heat absorbed by the phase change material during its transition is assumed to be linearly distributed over its melting range.

The convective heat transfer in the coolant channel is considered as a boundary condition for the thermal energy conservation equation at the channel-coolant interface, given as

$$k \frac{\partial T}{\partial x} = h_w \left(T_w - T_b\right) \tag{49}$$

where k (W m^{-1} K^{-1}) is the thermal conductivity of the channel, h_w (W m^{-2} K^{-1}) is convective heat transfer coefficient, T_w (K) is the channel wall temperature, and T_b (K)

is the bulk fluid temperature [60]. The local convective heat transfer coefficient, *h*, is calculated in each iteration by solving for the flow and temperature field in the coolant. This is done by numerically solving the Navier-Stokes equations for continuity and momentum using a finite volume discretization method and SIMPLE algorithm, given the constant velocity inlet and static pressure outlet boundary conditions [73].

4.3 Results and Discussion

A hybrid active/passive cooling system using chilled cold plates and phase change materials was modeled to determine the effects of discharge condition, PCM properties, cell spacing, PCM cap thickness and flow rate on the temperature and temperature gradient response of a 25 cell module. The relative effects of each of these constraints were studied along with the size and weight addition that a suitable BTMS requires. During the subsequent analysis, the conditions that are not being analyzed are kept at a constant base value. These controlled variables are external short discharge, paraffin wax PCM, 2 mm spacing, 2 mm cap thickness, and a coolant Reynolds number of 1125, corresponding to laminar pipe flow. Additionally, the initial temperature of the cells is specified as 25 °C, and the coolant inlet temperature is specified at 20 °C.

4.3.1 Discharge Conditions

Three loading conditions were tested in this work. The first is a constant current discharge at C/2, which completes in approximately two hours. This is a discharge that is generally considered to be a reasonable upper limit for “nominal” operation of small to medium sized batteries. Next is a constant current discharge at 3C, which completes full discharge in 20 minutes. Degradation and high heat generation would be experienced by

most cells discharged at this rate, unless they are specifically designed for such a rate. Last, the most extreme case of external short circuit is tested. This is modeled as a constant resistance of 100 mΩ applied to the module. Figure 22a shows the maximum temperature evolution for each discharge condition with time normalized to discharge capacity. For the C/2 discharge condition, the cells heat slightly to a maximum of 26 °C, but then steadily decline in temperature to a minimum value of 20 °C to match the coolant temperature. This result indicates that for low discharge rates, the active cooling system dominates and prevents the cells from reaching the melting temperature of the PCM. Next, for the 3C discharge, the cells heat steadily until about 2/3 into the discharge cycle when the cell temperature reaches the paraffin wax melting range of 42 to 45 °C. At this point the maximum temperature plateaus at 43 °C as the heat generated by the cells is absorbed by the latent heat of the PCM. The short circuit case also exhibits similar behavior, with the main difference being that the maximum cell temperature rises to nearly 45 °C before the phase change initiates, indicating that there is a significant difference between the core and surface temperatures of the cells. The maximum temperature gradients in the cell, shown in Figure 22b, show a similar trend as that of the maximum temperatures. The peak gradient values increases as the rate of discharge increases. Interestingly, in both the 3C and constant resistance simulations, the temperature gradient increase to a maximum and then decreases as the PCM begins to melt. The degree of melting for the PCM at the end of discharge is shown in Figure 23. It is clear that the C/2 case does not initiate phase transition, the short circuit case melts

the PCM significantly, and the 3C case is somewhere in between. Additionally, the cross-sectional temperature profiles during discharge are shown in Figure 24.

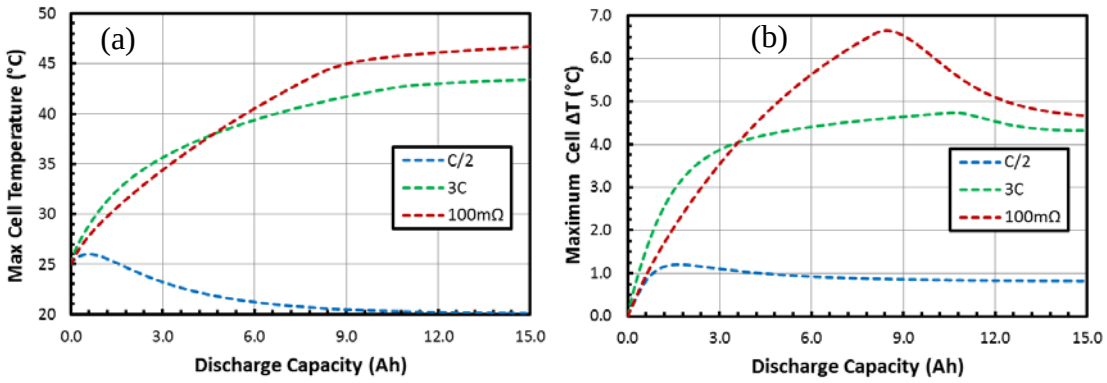

Figure 22. (a) Maximum cell temperature and (b) temperature gradient for nominal, high, and external short discharge conditions: constant current at C/2, constant current at 3C, and constant resistance at 100 mΩ. PCM is paraffin wax at 2mm spacing and cap with Re = 1125.

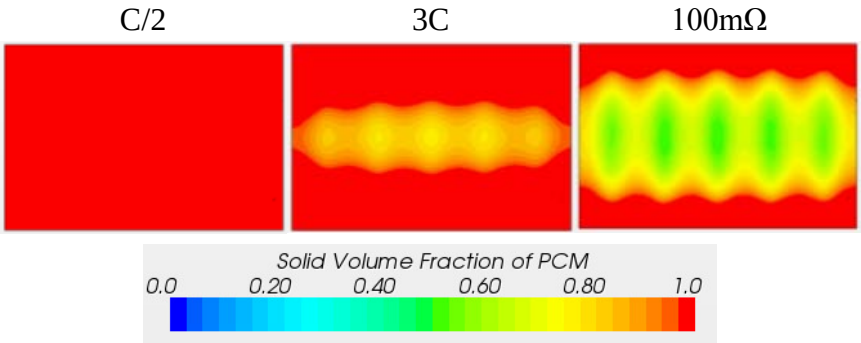

Figure 23. Cross-sectional solid volume fraction in the phase change material for three discharge conditions at the end of discharge. PCM is paraffin wax at 2 mm spacing and cap with Re = 1125.

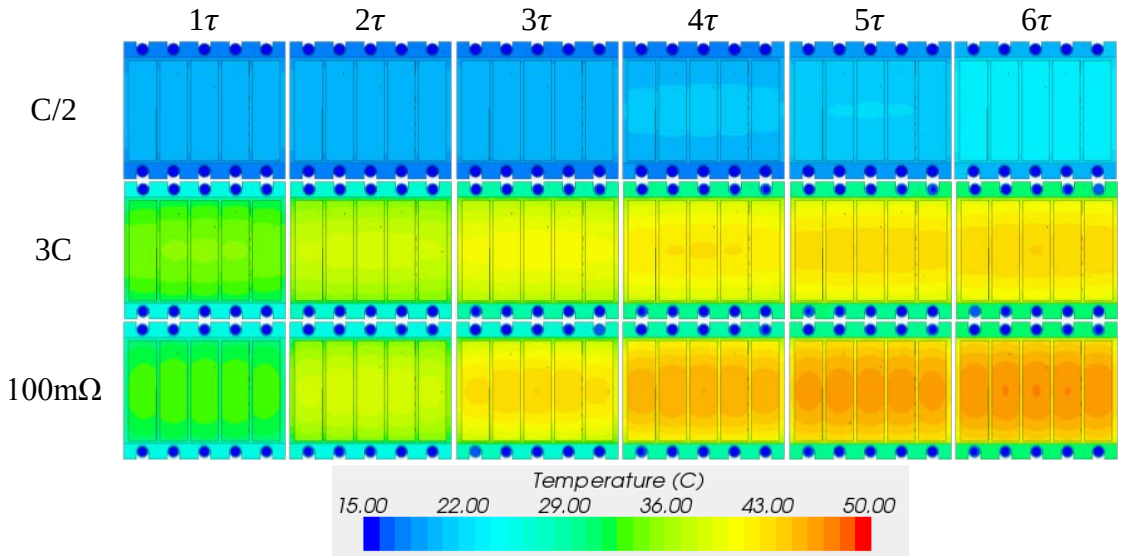

Figure 24. Cross-sectional temperature distributions for nominal, high, and external short discharge conditions during discharge. Time scale is non-dimensional. PCM is paraffin wax at 2 mm spacing and cap with Re = 1125.

These profiles show that the temperature gradients are highest in the vertical direction. This is likely due to the high dissipation rate provided by the cooling channel, and by the anisotropic thermal conductivity of the cells. Together these results show that under normal operating conditions, active cooling can maintain the cell temperatures near the coolant temperature. Additionally, the latent heat of the PCM prevents the cells from reaching the safety temperature limit even under abuse conditions, but does allow for the thermal gradients to break the recommended limit.

4.3.2 Phase Change Material

The thermo-physical properties of the phase change material have a very significant effect on the performance of the passive system. As shown in Figure 25a, the maximum cell temperature is kept completely below the safety limit of 50 °C for both lauric acid and paraffin wax. The lauric acid cell temperature rises faster than that of the paraffin wax due to its lower specific heat and thermal conductivity. Because of this, the lauric acid PCM reaches its melting point before paraffin wax and actually completely melts near the cells before the end of discharge, as indicated by the small rise in temperature past 13 Ah. Without the use of PCM, cell temperatures steeply rise to nearly 90 °C at the end of discharge, which is well beyond the safety limit. Figure 25b depicts the maximum cell thermal gradient which shows the onset of phase transition, indicated by the drop in thermal gradient for both PCMs. The thermal conductivity and latent heat seem to dominate the phase transition. The solid volume fraction, shown in Figure 26, indicates that the paraffin wax melts more evenly due to increased thermal conductivity whereas the lauric acid melts sooner due to its lower melting range. Overall, the paraffin wax decreases the maximum cell temperature but the lauric acid decreases the thermal gradient because of the differences in thermal conductivity and latent heat.

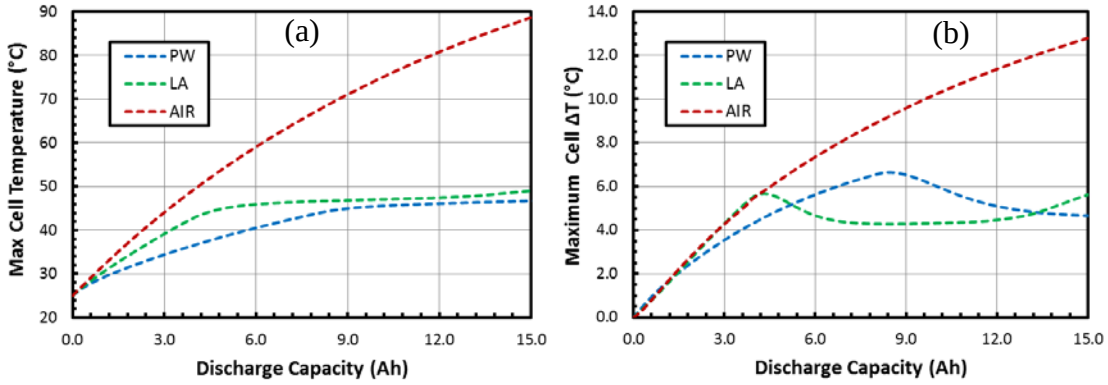

Figure 25. (a) Maximum cell temperature and (b) temperature gradient for paraffin wax, lauric acid, and a module with no PCM during constant resistance discharge at 100 mΩ. Spacing and cap are 2mm and Re = 1125.

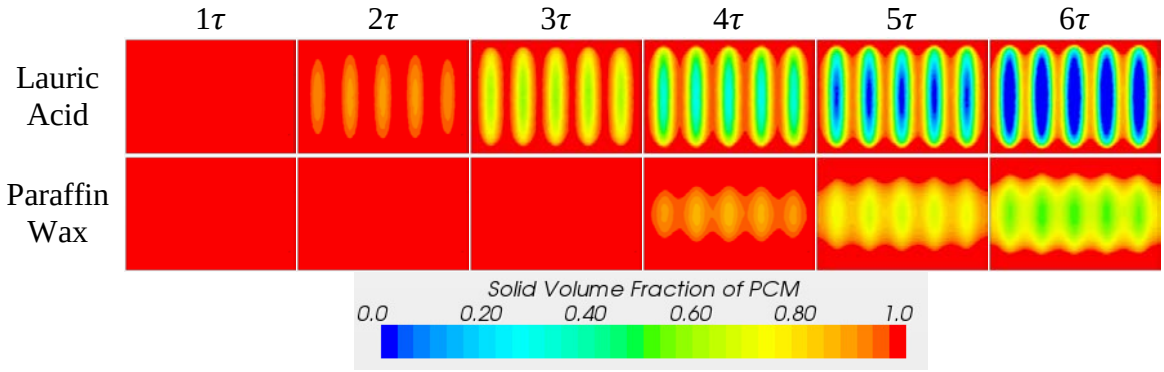

Figure 26. Cross-sectional solid volume fraction in the phase change material for lauric acid and paraffin wax during constant resistance discharge at 100 mΩ. Time scale is non-dimensional.

4.3.3 Cell Spacing

Shown in Figure 27a, the inter-cell spacing also has a large effect on maximum temperature. Increased spacing yields an increased PCM volume, permitting greater thermal energy storage and therefore decreased cell temperature. As shown in Figure 27b, the effect of spacing on cell thermal gradient is less straightforward. Increasing the spacing from 2 to 4 mm decreases the gradient, but increasing further to 6 mm raises the temperature difference back up. This indicates that the optimum PCM spacing is near 4 mm.

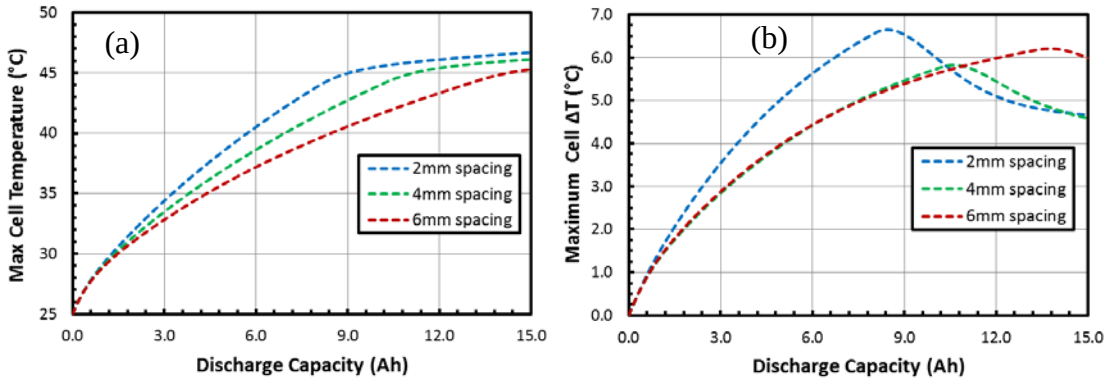

Figure 27. (a) Maximum cell temperature and (b) temperature gradient for 2, 4, and 6 mm spacing between the cells with paraffin wax PCM during constant resistance discharge at 100 mΩ. Cap thickness was set to 2mm, and the coolant Re = 1125.

4.3.4 PCM Cap Thickness

The effect of cap thickness is less apparent than that of cell spacing. Figure 28a shows that increasing the thickness of the PCM cap only slightly increases maximum temperature, which is undesirable. However, increasing the cap thickness does decrease the maximum temperature gradient shown in Figure 28b. This is because a thicker cap increases the heat transfer resistance to the cold plate. This effect can also be achieved by decreasing the flow rate of the coolant. These results show that the usefulness of a PCM cap is limited to when only passive cooling is used, and is actually counter-productive when placed between the cells and a cold plate.

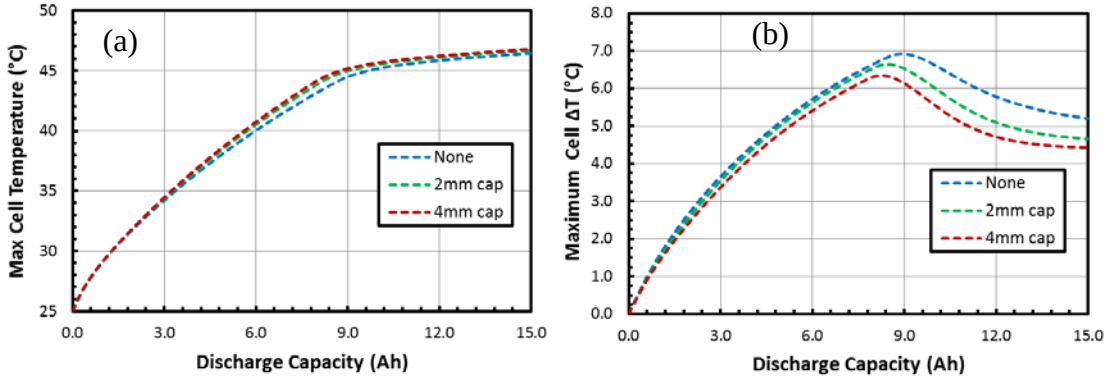

Figure 28. (a) Maximum cell temperature and (b) temperature gradient for 0, 2, and 4 mm cap thickness between the cells and the cold plate with paraffin wax PCM during constant resistance discharge at 100 mΩ. Spacing was held at 2mm and the coolant Re = 1125.

4.3.5 Power Requirements

Figure 29 shows the effect of flow Reynolds number on the power requirement and Nusselt number for this simulation. As expected, the increase of pumping power requirement with increase of Reynolds number approximately follows a power law relationship. Conversely, the Nusselt number follows a logarithmic relationship with Reynolds number. Figure 30 shows the cross-sectional temperature profile in the module at the end of discharge for three flow rates. This shows that the effect of flow rate on module temperature is slight to negligible. It can be drawn from these results that increasing the coolant flow rate is not desired unless the module temperature is approaching the safety limit. As the power requirement for active BTMS is often drawn from the battery itself, it is desirable to minimize power. The active system can potentially be disabled until the cells reach a temperature closer to the safety limit to save on power. In summary, the flow rate of the active cooling system does not significantly affect the cooling performance. It is likely that at the system level, radiator design will have a large effect on the active cooling system performance, as the inlet temperature could fluctuate.

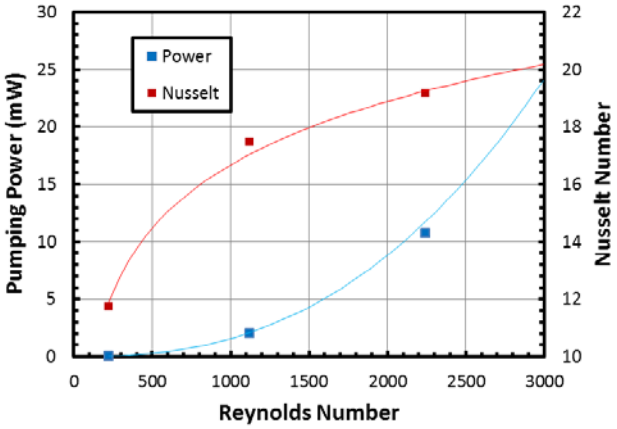

Figure 29. Pump power requirement and Nusselt number for Reynolds numbers of 225, 1125, and 2250. Results calculated from coolant channel geometry with water as the coolant at steady flow conditions.

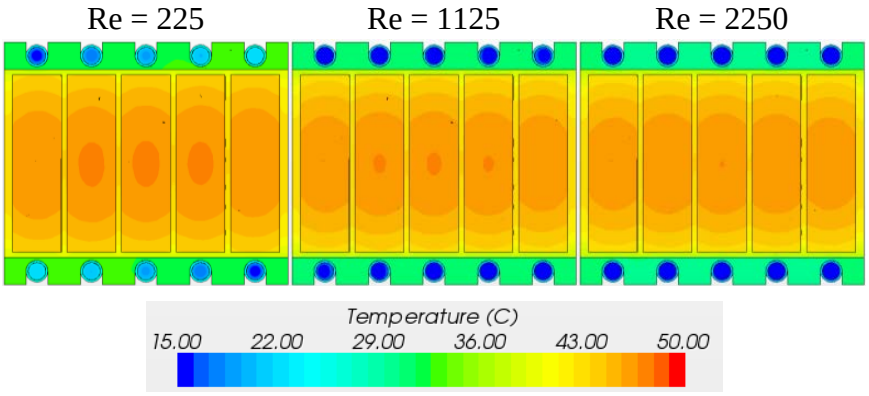

Figure 30. Cross-sectional temperature distributions for Reynolds numbers of 225, 1125, and 2250 at the end of constant resistance discharge at 100 mΩ. Spacing and cap thickness set to 2mm.

4.4 Summary

This work uses a coupled electrochemical-thermal numerical modeling approach to determine the effect of design considerations such as discharge condition, PCM properties, inter-cell spacing, and material cap thickness on the maximum temperature and thermal gradient. Under normal operating conditions, active cooling can maintain the cell temperatures near the coolant temperature. In addition, the latent heat of the PCM prevents the cells from reaching the safety temperature limit even under abuse conditions, but does allow for the thermal gradients to break the recommended limit. Paraffin wax decreases the maximum cell temperature but lauric acid decreases the thermal gradient because of the differences in thermal conductivity and latent heat, indicating that PCM properties have a large effect on their effectiveness as a cooling system. It was also found that cell spacing between 2 and 4 mm is preferred and a cap between the cells and cold plate is undesirable. This configuration leads to a 55% increase in weight and a 60% increase in volume, which is reasonable considering the substantial increase in safety over a module with no BTMS. Lastly, the coolant flow rate has little effect on the temperature of the module, provided that the cold plate is in good thermal contact with the cells. When combined with the use of cell-level safety devices and rigorous cell screening, a passive or hybrid battery thermal management system using a PCM significantly reduces the risk of catastrophic module failure at a modest increase in size and mass.

5. CONCLUSIONS AND RECOMMENDATIONS

In the present work the thermal behavior of lithium-ion batteries under abuse conditions was analyzed using both experimental and numerical techniques. First, the single-cell thermal response of LIBs subjected to heat-to-vent tests using a constant power heater was characterized. It was found that, when adjusted for thermal mass, cells of the same chemistry responded nearly the same to the heat-to-vent test. The main behavioral difference in the cylindrical and prismatic cells that were tested was in the activation of their safety vents. In general, the cylindrical 18650 cells vented at a consistent temperature and did not experience electrolyte ignition, whereas the vented electrolyte from the prismatic cells did ignite, causing more damage than in the cylindrical tests. In addition, an existing thermal abuse model for oven tests was modified to accurately predict the reaction behavior during the single-cell heat-to-vent test. This model showed that the negative- and positive-solvent reactions were the most significant during the onset of thermal runaway, but the electrolyte decomposition and combustion contributed the most to the sustained heating of the cells. Lastly, it was shown that increasing the rate convective heat transfer can slow or even stop thermal runaway. The results indicate that locating a less reactive electrolyte that still maintains suitable performance will greatly improve the safety of LIBs. In the future, the developed constant-flux heating model can be used to predict the thermal behavior of large battery modules in a reaction kinetics framework.

Next, the thermal behavior of LIB modules subjected to the same constant-power heating abuse test was analyzed experimentally. The effect of module design parameters including cell spacing, tabbing style, and vent location on thermal runaway propagation determined. Intuitively, increasing the separation between cells decreased the chance and severity of thermal runaway in cells adjacent to the abused cell. Additionally, it was found that parallel banks of cells were generally more reactive than series strings, due to the external short circuit caused by the abused cell in parallel configuration. The tabbing style also played an important role in damage propagation, as serpentine tabs caused the modules to electrically drain more than branched tabs. Lastly, the radiant barrier and intumescent thermal insulation materials sufficiently protected neighboring cells from impinging electrolyte flames. Based on these experiments, it is recommended that cells be spaced a minimum of 2 mm from each other and that parallel tabs should be designed such that a short in one cell does not affect the rest of the bank. Insulation materials are recommended for module configurations where electrolyte vapors can be directed toward a neighboring cell to mitigate the propagation of thermal runaway.

Lastly, an electrochemical-thermal model of a hybrid active/passive battery thermal management system was developed. The effect of cell spacing, phase change material properties, and coolant flow rate were studied. It was found that increasing cell spacing significantly decreased the temperature of a twenty-five cell module under external short-circuit conditions. Additionally, increasing the PCM thermal conductivity and latent heat storage decreases the module temperature rise under abuse conditions. The combined cooling effect of the active cooling system and the passive phase change

material latent heat maintained the module temperature well below the safety limit of 50 °C under short circuit conditions. The paraffin wax PCM decreased the maximum cell temperature but the lauric acid PCM decreased the thermal gradient because of the differences in thermal conductivity and latent heat, indicating that PCM properties have a large effect on their effectiveness as a cooling system. It was also found that the coolant flow rate had only a small effect on the temperature response of the cells, whereas inlet temperature is expected to contribute more. While the addition of the hybrid management system greatly improved the module safety, it comes at a cost of a 55% increase in weight and a 60% increase in volume. It is recommended that designers carefully consider using hybrid battery thermal management systems when safety is paramount.

NOMENCLATURE

Abbreviations

BTMS	Battery Thermal Management System
CID	Current Interrupt Device
DOD	Depth of Discharge
LIB	Lithium-Ion Battery
OCV	Open Circuit Voltage/Potential
PTC	Positive Temperature Coefficient
SOC	State of Charge

Symbols

a	Equilibrium voltage fit coefficients (V)
A_s	Electrode surface area (m^2)
A	Area (m^2)
A_e	Electrolyte decomposition frequency factor (s^{-1})
A_{ne}	Negative-solvent frequency factor (s^{-1})
A_{pe}	Positive-solvent frequency factor (s^{-1})
A_{sei}	SEI-decomposition frequency factor (s^{-1})
b	Conductance fit coefficients ($S\ m^{-2}$)
c	Voltage-temperature correction coefficient ($V\ K^{-1}$)
C	Dimensionless distance
c_e	Concentration of electrolyte

c_i	Reactant concentration
c_{ne}	Amount of lithium in the carbon
c_p	Heat capacity (J kg^{-1} K^{-1})
c_{sei}	Amount of lithium-containing meta-stable species in the SEI
E_a	Activation energy (J mol^{-1})
$E_{a,e}$	Electrolyte decomposition activation energy (J mol^{-1})
$E_{a,ne}$	Negative-solvent activation energy (J mol^{-1})
$E_{a,pe}$	Positive-solvent activation energy (J mol^{-1})
$E_{a,sei}$	SEI-decomposition activation energy (J mol^{-1})
F_{12}	View factor
h	Heat transfer coefficient (W m^{-2} K^{-1})
H_e	Electrolyte decomposition heat (J kg^{-1})
h_{latent}	Latent heat of fusion (J kg^{-1})
h_{ls}	Liquid-solid enthalpy (J kg^{-1})
H_{ne}	Negative-solvent heat (J kg^{-1})
H_{pe}	Positive-solvent heat (J kg^{-1})
h_s	Sensible heat (J kg^{-1})
H_{sei}	SEI-decomposition heat (J kg^{-1})
h_w	Convective heat transfer coefficient (W m^{-2} K^{-1})
I	Current (A)
J	Current density (A m^{-2})
k	Thermal conductivity (W m^{-1} K^{-1})

l	Thickness (m)
m	Reaction order
m_e	Reaction order for c_e
m_{pe1}	Reaction order for α
m_{pe2}	Reaction order for (1- α)
m_{sei}	Reaction order for c_{sei}
Q	Total heat generation rate (W m^{-3})
Q_{cond}	Conduction heat transfer rate (W)
q''_{conv}	Heat dissipation rate (W m^{-2})
Q_e	Electrolyte decomposition heat generation rate (W m^{-3})
Q_{gen}	Heat generation rate (W m^{-3})
Q_{ne}	Negative-solvent heat generation rate (W m^{-3})
Q_{pe}	Positive-solvent heat generation rate (W m^{-3})
Q_{rad}	Radiation heat transfer rate (W)
Q_{sei}	SEI-decomposition heat generation rate (W m^{-3})
r	Cell radius (m)
R	Universal gas constant (J mol^{-1} K^{-1})
R_e	Electrolyte decomposition rate (J kg^{-1})
R_i	Reaction rate
R_{ne}	Negative-solvent rate (J kg^{-1})
R_{pe}	Positive-solvent rate (J kg^{-1})
R_{sei}	SEI-decomposition rate (J kg^{-1})

s	Source term
T	Temperature (K)
t	Time (s)
T'	Normalized temperature
T_{amb}	Oven temperature (K)
T_b	Bulk fluid temperature (K)
T_{liq}	Liquidus temperature (K)
T_{ref}	Reference temperature (K)
T_{sol}	Solidus temperature (K)
T_{surf}	Cell surface temperature (K)
T_w	Wall surface temperature (K)
U	Equilibrium voltage (V)
v	Velocity (m s^{-1})
V	Volume (m^3)
V_{cell}	Cell voltage (V)
W_c	Carbon content (kg m^{-3})
W_e	Electrolyte content (kg m^{-3})
W_p	Active material content in cathode (kg m^{-3})
x	Distance
Y	Conductance (S m^{-2})

Greek

α	Degree of conversion
α_i	Phase volume fraction
α_s	Solid volume fraction
ε	Emissivity
μ	Viscosity (Pa s)
ρ	Density (kg m^{-3})
σ	Stefan-Boltzmann constant (W m^{-2} K^{-4})

REFERENCES

1. T. M. Bandhauer, S. Garimella and T. F. Fuller, *J Electrochem Soc*, **158**, R1 (2011).

2. W. T. J. A. Jeevarajan, Performance and Safety Tests of Lithium-Ion Cells Arranged in a Matrix Design Configuration, in *Space Power Workshop*, Manhattan Beach, CA (2010).

3. J. A. Jeevarajan, Safety Limitations Associated with Commercial 18650 Lithium-ion Cells, in, NASA, Johnson Space Center (2010).

4. T. Reddy, *Linden's Handbook of Batteries*, McGraw-Hill Professional (2010).

5. D. Belov and M. H. Yang, *Solid State Ionics*, **179**, 1816 (2008).

6. T. Ohsaki, T. Kishi, T. Kuboki, N. Takami, N. Shimura, Y. Sato, M. Sekino and A. Satoh, *J Power Sources*, **146**, 97 (2005).

7. Q. S. Wang, P. Ping, X. J. Zhao, G. Q. Chu, J. H. Sun and C. H. Chen, *J Power Sources*, **208**, 210 (2012).

8. P. G. Balakrishnan, R. Ramesh and T. P. Kumar, *J Power Sources*, **155**, 401 (2006).

9. D. H. Doughty, E. P. Roth, C. C. Crafts, G. Nagasubramanian, G. Henriksen and K. Amine, *J Power Sources*, **146**, 116 (2005).

10. M. Kise, S. Yoshioka and H. Kuriki, *J Power Sources*, **174**, 861 (2007).

11. K. Zaghib, J. Dube, A. Dallaire, K. Galoustov, A. Guerfi, M. Ramanathan, A. Benmayza, J. Prakash, A. Mauger and C. M. Julien, *J Power Sources*, **219**, 36 (2012).

12. E. P. Roth and D. H. Doughty, *J Power Sources*, **128**, 308 (2004).

13. J. A. Jeevarajan, Hazards, Safety and Design Considerations for Commercial Lithium-ion Cells and Batteries, in *2nd International Association for the Advancement of Space Safety*, NASA, Johnson Space Center, Chicago, IL (2007).

14. M. S. Wu, P. C. J. Chiang, J. C. Lin and Y. S. Jan, *Electrochim Acta*, **49**, 1803 (2004).

15. S. Tobishima, K. Takei, Y. Sakurai and J. Yamaki, *J Power Sources*, **90**, 188 (2000).

16. D. H. Doughty, P. C. Butler, R. G. Jungst and E. P. Roth, *J Power Sources*, **110**, 357 (2002).

17. K. Smith, G. H. Kim, E. Darcy and A. Pesaran, *Int J Energ Res*, **34**, 204 (2010).

18. W. B. Gu and C. Y. Wang, *J Electrochem Soc*, **147**, 2910 (2000).

19. G. H. Kim, K. Smith, K. J. Lee, S. Santhanagopalan and A. Pesaran, *J Electrochem Soc*, **158**, A955 (2011).

20. R. Spotnitz and J. Franklin, *J Power Sources*, **113**, 81 (2003).

21. M. N. Richard and J. R. Dahn, *J Electrochem Soc*, **146**, 2068 (1999).

22. H. Maleki, G. P. Deng, A. Anani and J. Howard, *J Electrochem Soc*, **146**, 3224 (1999).

23. D. D. MacNeil, D. Larcher and J. R. Dahn, *J Electrochem Soc*, **146**, 3596 (1999).

24. P. Biensan, B. Simon, J. P. Peres, A. de Guibert, M. Broussely, J. M. Bodet and F. Perton, *J Power Sources*, **81**, 906 (1999).

25. D. D. MacNeil and J. R. Dahn, *J Electrochem Soc*, **148**, A1205 (2001).

26. D. D. MacNeil, Z. H. Lu, Z. H. Chen and J. R. Dahn, *J Power Sources*, **108**, 8 (2002).

27. W. H. Kong, H. Li, X. J. Huang and L. Q. Chen, *J Power Sources*, **142**, 285 (2005).

28. G. G. Botte, R. E. White and Z. M. Zhang, *J Power Sources*, **97-8**, 570 (2001).

29. T. Kawamura, A. Kimura, M. Egashira, S. Okada and J. I. Yamaki, *J Power Sources*, **104**, 260 (2002).

30. T. D. Hatchard, D. D. MacNeil, A. Basu and J. R. Dahn, *J Electrochem Soc*, **148**, A755 (2001).

31. T. D. Hatchard, D. D. MacNeil, D. A. Stevens, L. Christensen and J. R. Dahn, *Electrochem Solid St*, **3**, 305 (2000).

32. G. H. Kim, A. Pesaran and R. Spotnitz, *J Power Sources*, **170**, 476 (2007).

33. G. F. Guo, B. Long, B. Cheng, S. Q. Zhou, P. Xu and B. G. Cao, *J Power Sources*, **195**, 2393 (2010).

34. R. M. Spotnitz, J. Weaver, G. Yeduvaka, D. H. Doughty and E. P. Roth, *J Power Sources*, **163**, 1080 (2007).

35. P. Peng, Y. Q. Sun and F. M. Jiang, *Heat Mass Transfer*, **50**, 1405 (2014).

36. B. K. Mandal, A. K. Padhi, Z. Shi, S. Chakraborty and R. Filler, *J Power Sources*, **161**, 1341 (2006).

37. Y. E. Hyung, D. R. Vissers and K. Amine, *J Power Sources*, **119**, 383 (2003).

38. C. Y. Jhu, Y. W. Wang, C. Y. Wen and C. M. Shu, *Appl Energ*, **100**, 127 (2012).

39. H. Yang, H. Bang, K. Amine and J. Prakash, *J Electrochem Soc*, **152**, A73 (2005).

40. C. Y. Wen, C. Y. Jhu, Y. W. Wang, C. C. Chiang and C. M. Shu, *J Therm Anal Calorim*, **109**, 1297 (2012).

41. P. Ribiere, S. Grugeon, M. Morcrette, S. Boyanov, S. Laruelle and G. Marlair, *Energ Environ Sci*, **5**, 5271 (2012).

42. G. Bertelli, G. Camino, E. Marchetti, L. Costa, E. Casorati and R. Locatelli, *Polym Degrad Stabil*, **25**, 277 (1989).

43. G. Camino, L. Costa and G. Martinasso, *Polym Degrad Stabil*, **23**, 359 (1989).

44. S. Bourbigot, M. Le Bras, S. Duquesne and M. Rochery, *Macromol Mater Eng*, **289**, 499 (2004).

45. S. Bourbigot, M. Le Bras, F. Dabrowski, J. W. Gilman and T. Kashiwagi, *Fire Mater*, **24**, 201 (2000).

46. B. K. Kandola and A. R. Horrocks, *Polym Degrad Stabil*, **54**, 289 (1996).

47. B. Li and M. J. Xu, *Polym Degrad Stabil*, **91**, 1380 (2006).

48. J. W. Gu, G. C. Zhang, S. L. Dong, Q. Y. Zhang and J. Kong, *Surf Coat Tech*, **201**, 7835 (2007).

49. M. Bugajny, M. Le Bras and S. Bourbigot, *J Fire Sci*, **18**, 7 (2000).

50. E. G. Shim, T. H. Nam, J. G. Kim, H. S. Kim and S. I. Moon, *J Power Sources*, **172**, 919 (2007).

51. J. A. Jeevarajan, Validation of Battery Safety For Space Missions, in, NASA - Johnson Space Center (2012).

52. B. S., J. Jeevarajan, T. Nelson, Performance and Safety Evaluation of High-rate 18650 Lithium-Iron-Phosphate Cells, in, NASA Battery Workshop (2009).

53. S. Al-Hallaj and J. R. Selman, *J Power Sources*, **110**, 341 (2002).

54. Y. Troxler, B. Wu, M. Marinescu, V. Yufit, Y. Patel, A. J. Marquis, N. P. Brandon and G. J. Offer, *J Power Sources*, **247**, 1018 (2014).

55. Y. Ji, Y. C. Zhang and C. Y. Wang, *J Electrochem Soc*, **160**, A636 (2013).

56. M. K. A. Pesaran, G. Kim, S. Santhanagopalan, K. Smith, Tools for Designing Thermal Management of Batteries in Electric Drive Vehicles, in, NREL (2013).

57. R. Sabbah, R. Kizilel, J. R. Selman and S. Al-Hallaj, *J Power Sources*, **182**, 630 (2008).

58. A. A. Pesaran, S. Burch and M. Keyser, *Vtms 4: Vehicle Thermal Management Systems*, 331 (1999).

59. S. A. Khateeb, M. M. Farid, J. R. Selman and S. Al-Hallaj, *J Power Sources*, **128**, 292 (2004).

60. T. L. Bergman and F. P. Incropera, *Fundamentals of heat and mass transfer*, p. xxiii, John Wiley & Sons, Hoboken, NJ (2011).

61. Z. Y. Ling, J. J. Chen, X. M. Fang, Z. G. Zhang, T. Xu, X. N. Gao and S. F. Wang, *Appl Energ*, **121**, 104 (2014).

62. Z. Y. Ling, Z. G. Zhang, G. Q. Shi, X. M. Fang, L. Wang, X. N. Gao, Y. T. Fang, T. Xu, S. F. Wang and X. H. Liu, *Renew Sust Energ Rev*, **31**, 427 (2014).

63. A. Sari and A. Karaipekli, *Appl Therm Eng*, **27**, 1271 (2007).

64. M. Y. Ramandi, I. Dincer and G. F. Naterer, *Heat Mass Transfer*, **47**, 777 (2011).

65. A. Mills and S. Al-Hallaj, *J Power Sources*, **141**, 307 (2005).

66. R. Ehid and A. S. Fleischer, *Energ Convers Manage*, **53**, 84 (2012).

67. B. Zalba, J. M. Marin, L. F. Cabeza and H. Mehling, *Appl Therm Eng*, **23**, 251 (2003).

68. C. M. Jiao, B. H. Ji and D. Fang, *Mater Lett*, **67**, 352 (2012).

69. V. Ramadesigan, P. W. C. Northrop, S. De, S. Santhanagopalan, R. D. Braatz and V. R. Subramanian, *J Electrochem Soc*, **159**, R31 (2012).

70. U. S. Kim, C. B. Shin and C. S. Kim, *J Power Sources*, **189**, 841 (2009).

71. CD-adapco, Battery Design Studio Professional © User Guide, in, 9.04.009 ed. (2014).

72. P. P. Mukherjee, S. Pannala and J. A. Turner, *Handbook of Battery Materials, 2nd Edition*, 843 (2011).

73. CD-adapco, STAR-CCM+ © User Guide, in, 9.04.009 ed. (2014).

74. J. Newman and W. Tiedemann, *J Electrochem Soc*, **140**, 1961 (1993).

75. H. Gu, *J Electrochem Soc*, **130**, 1459 (1983).

76. M. Doyle, T. F. Fuller and J. Newman, *J Electrochem Soc*, **140**, 1526 (1993).

77. J. U. Brackbill, D. B. Kothe and C. Zemach, *J Comput Phys*, **100**, 335 (1992).

78. M. P. S. Muzaferija, in *Nonlinear Water Wave Interaction*, O. and M. a. M. Markiewicz Editors, Computational Mechanics Publications, WIT Press, Southampton (1999).

79. A. Teskeredzic, I. Demirdzic and S. Muzaferija, *Numer Heat Tr B-Fund*, **42**, 437 (2002).

80. C. R. Swaminathan and V. R. Voller, *Int J Heat Mass Tran*, **40**, 2859 (1997).

81. C. R. Swaminathan and V. R. Voller, *Metall Trans B*, **23**, 651 (1992).

82. C. M. Oldenburg and F. J. Spera, *Numer Heat Tr B-Fund*, **21**, 217 (1992).